Molecular Dynamics Simulation of Water between Metal Walls under Electric Field: Dielectric Response and Dynamics after Field Reversal

Kyohei Takae[1] and Akira Onuki[2]
[1] *Institute of Industrial Science, University of Tokyo, 4-6-1 Komaba, Meguro-ku, Tokyo 153-8505, Japan*
[2] *Department of Physics, Kyoto University, Kyoto 606-8502, Japan*
(Dated: March 10, 2015)

We study water between parallel metal walls under applied electric field accounting for the image effect at $T = 298$ K. The electric field due to the surface charges serves to attract and orient nearby water molecules, while it tends to a constant determined by the mean surface charge density away from the walls. We find Stern boundary layers with thickness about 5 Å and a homogeneously polarized bulk region. The molecules in the layers more sensitively respond to the applied field than in the bulk. As a result, the potential drop in the layers is larger than that in the bulk unless the cell length exceeds 10 nm. We also examine the hydrogen bonds, which tend to make small angles with respect to the walls in the layers even without applied field. The average local field considerably deviates from the classical Lorentz field and the local field fluctuations are very large in the bulk. If we suppose a nanometer-size sphere around each molecule, the local field contribution from its exterior is nearly equal to that from the continuum electrostatics and that from its interior yields the deviation from the classical Lorentz field. As a nonequilibrium problem, we investigate the dynamics after a reversal of applied field, where the relaxation is mostly caused by large-angle rotational jumps after 1 ps due to the presence of the hydrogen bond network. The molecules undergoing these jumps themselves form hydrogen-bonded clusters heterogeneously distributed in space.

arXiv:1410.7146v2 [cond-mat.soft] 8 Mar 2015

I. INTRODUCTION

In physics and chemistry, we need to accurately estimate the long-range electrostatic interactions among charged and polar particles. To this end, a large number of simulations have been performed and the Ewald method is a famous technique for efficiently summing these interactions using the Fourier transformation[1]. It has been used to investigate the bulk properties of charged and polar particles under the periodic boundary condition in three dimensions (3D Ewald)[2,3]. It has also been modified for film-like systems under the periodic boundary condition in the lateral directions (2D Ewald)[4–8]. Several groups[8–14] have performed simulations of dipole systems in electric field between parallel metal walls. However, not enough efforts have been made on dynamics, where applied electric field can be nonstationary. Such nonequilibrium situations are ubiquitous and are of great scientific and practical importance. Hence, this paper aims to give a general scheme of treating water under electric field and investigate the dielectric relaxation after field reversal.

Hautman et al.[9] developed a 3D Ewald method assuming parallel, smooth metal walls, where the constant potential condition is satisfied at the metal walls ($z = 0$ and H) and the periodic boundary condition is imposed along the x and y axes. In this case, each charged particle in the cell induces surface charges producing a potential equivalent to that from an infinite number of image charges outside the cell. Perram and Ratner[10] found some relations on these image charges. In the same scheme, Klapp[11] treated dipoles interacting with the soft-core potential to find wall-induced ordering. The present authors[12] extended this 3D Ewald method for charged and polar particles to examine surface effects, ionic crystals, dipole chains, and local electric field. In this paper, we use this method for water.

We also mention other methods. Shelley and Patey[15] assumed empty (vacuum) slabs outside the cell, which the particles cannot enter due to the repulsive wall potentials. If the regions $-d_{\rm em} < z < 0$ and $H < z < H + d_{\rm em}$ are empty, the 3D Ewald method can be used with period $H + 2d_{\rm em}$ along the z axis. Also with empty slabs, Yeh and Berkowitz[13] applied electric field accounting for the local field from net polarization. They found that the computing time with this 3D Ewald method was ten times faster than that with the 2D Ewald method. With such empty regions, however, charged or polar particles are effectively in contact with neutral, non-polarizable walls. Siepmann and Sprik[16] assumed atomic particles forming a crystal and interacting with water molecules via a model potential at the surface. They varied charges of these atoms continuously to maintain the constant potential condition in metal. This model was used to study water and ions between electrodes with the aid of the 2D Ewald method[14,17]. Petersen *et al.*[18] proposed an efficient simulation method accounting for the primary image charges closest to the boundary walls and uniform (average) surface charge densities.

Surface charges increase locally as charges or dipoles in the liquid region approach a metal wall. As a result, water molecules are adsorbed and oriented near a metal wall[19–21]. They form a Stern surface layer[22,23] even without ions, where the electric potential changes appreciably on a microscopic length. It also follows that the surface charges exhibit significant in-plane fluctuations with a

correlation length ξ_s. We shall see that the electric field due to these surface charges tends to be uniform in the bulk where the distances from the walls much exceeds ξ_s.

We are not aware of previous microscopic calculations to check the validity of the classical theory of dielectrics[24–26]. Hence, we calculate the average and fluctuations of the local electric field $\boldsymbol{E}_k^{\rm loc}$ acting on each molecule k. In particular, we consider a nanometer-size sphere surrounding each molecule. In our simulation, the local field contribution from the sphere interior consists of an average (a deviation from the classical Lorentz field) and large fluctuations ($\sim e/\sigma^2$ with $\sigma \sim 3$ Å), while that from the sphere exterior is obtained from the continuum electrostatics with small fluctuations.

We also present a first study of nonequilibrium water, where the polarization relaxes after a reversal of applied electric field. In this relaxation, rotational jumps with large angle changes play a major role. These largely rotated molecules form clusters causing breakage and reorganization of the hydrogen bond network. In previous simulations on water, collective hydrogen-bond dynamics was studied at $T \sim 300$ K[27,28] and marked dynamic heterogeneities were observed in translation and rotation in supercooled states[29,30].

The organization of this paper is as follows. In Sec. II, we will reexamine the Ewald scheme for water between metal walls. In Sec. III, we will calculate the dielectric response and the local electric field. In Sec.IV, simulation results on field reversal will be presented. In Appendix A, we will give an expression for the local electric field on water molecules composed of three charge points. In Appendix B, we will devise a microscopic expression for the polarization density $\boldsymbol{p}(\boldsymbol{r})$, which is convenient for theoretical study of water.

II. THEORETICAL BACKGROUND

A. Water Model. We use the TIP4P/2005 model[31], where each water molecule k has three charge points $\boldsymbol{r}_{k\rm H1}$, $\boldsymbol{r}_{k\rm H2}$, and $\boldsymbol{r}_{k\rm M}$ with fixed partial charges $q_{\rm H}$, $q_{\rm H}$, and $q_{\rm M} = -2q_{\rm H}$, respectively, where $q_{\rm H} = 0.5564e$. The point $\boldsymbol{r}_{k\rm M}$ is slightly shifted from the oxygen point $\boldsymbol{r}_{k\rm O}$ along $\boldsymbol{n}_k$, where $\boldsymbol{n}_k$ is the unit vector along the bisector of the H-O-H triangle. Its dipole moment is given by

$$\boldsymbol{\mu}_k = q_{\rm H}(\boldsymbol{r}_{k\rm H1} + \boldsymbol{r}_{k\rm H2} - 2\boldsymbol{r}_{k\rm M}) = \mu_0 \boldsymbol{n}_k, \tag{1}$$

where $\mu_0 = 2.305$D. See Appendix A for more details. We adopt this fixed charge model because of its simplicity, though the molecular polarizability is known to play a fundamental role in the properties of water[32,33].

The total potential U consists of three parts as

$$U = U_{\rm m} + \frac{1}{2}\sum_{k\neq\ell} u_{LJ}(|\boldsymbol{r}_{k\rm O} - \boldsymbol{r}_{\ell\rm O}|) + \sum_k [u_{\rm w}(z_{k\rm O}) + u_{\rm w}(H - z_{k\rm O})], \tag{2}$$

where $U_{\rm m}$ is the total electrostatic energy, $u_{\rm LJ}$ is the Lennard-Jones potential among the oxygen atoms, and $u_{\rm w}$ is the wall potential of the oxygen atoms:

$$u_{\rm LJ}(r) = 4\epsilon[(\sigma/r)^{12} - (\sigma/r)^6], \tag{3}$$

$$u_{\rm w}(z) = C_9(\sigma/z)^9 - C_3(\sigma/z)^3. \tag{4}$$

We set $\epsilon = 93.2k_B$, $\sigma = 3.1589$Å, $C_9 = 2\pi\epsilon/45$, and $C_3 = 15C_9/2 = \pi\epsilon/3$. Then, the elementary charge is given by $e = 23.82(\epsilon\sigma)^{1/2}$. Due to $u_{\rm w}(z)$ distances of any charge positions from the walls at $z = 0$ and H are larger than 1 Å. The density and the orientation of water molecules near a wall sensitively depend on the form of $u_{\rm w}(z)$.

In the literature, extensive efforts have been made to examine surface states of water using various simulation methods[14,16–21,34,35]. We also remark that ab initio models are needed to accurately describe the surface potentials on short length scales for water[36].

B. Electrostatic Energy and Image Charges. We consider a $L \times L \times H$ cell with metal plates at $z = 0$ and H using the periodic boundary condition along the x and y axes. Its volume is $V = L^2H$. The walls at $z = 0$ and H are assumed to be smooth and structureless for simplicity. We apply electric field under the fixed-potential condition.

Let $\boldsymbol{r}_i = (x_i, y_i, z_i)$ and $\boldsymbol{r}_j = (x_j, y_j, z_j)$ denote the 3N charge positions $\boldsymbol{r}_{k\rm H1}$, $\boldsymbol{r}_{k\rm H2}$, and $\boldsymbol{r}_{k\rm M}$ ($1 \le k \le N$). The electrostatic potential $\Phi(\boldsymbol{r})$ outside the charge positions $\boldsymbol{r} \neq \boldsymbol{r}_i$ satisfies the metallic boundary condition,

$$\Phi(x, y, 0) = 0, \quad \Phi(x, y, H) = -\Delta\Phi = -E_a H, \tag{5}$$

where $\Delta\Phi$ is the applied potential difference and $E_a = \Delta\Phi/H$ is the applied electric field. From eq 5, $\Phi(\boldsymbol{r})$ is expressed in terms of image charges as

$$\Phi = \sum_{\boldsymbol{m}}\sum_j \left[\frac{q_j}{|\boldsymbol{r} - \boldsymbol{r}_j + \boldsymbol{h}|} - \frac{q_j}{|\boldsymbol{r} - \bar{\boldsymbol{r}}_j + \boldsymbol{h}|}\right] - E_a z, \tag{6}$$

where $\bar{\boldsymbol{r}}_j = (x_j, y_j, -z_j)$ and

$$\boldsymbol{h} = (Lm_x, Lm_y, 2Hm_z) \tag{7}$$

with m_x, m_y, and m_z being integers $(0, \pm1, \pm2, ...)$. For each real charge q_j at $\boldsymbol{r}_j = (x_j, y_j, z_j)$ in the cell, we find images with the same charge q_j at $(x_j, y_j, z_j - 2Hm_z)$ $(m_z = \pm1, \cdots)$ and those with the opposite charge $-q_j$ at $(x_j, y_j, -z_j - 2Hm_z)$ $(m_z = 0, \pm1, \cdots)$ outside the cell. Due to the summation over m_z the metallic boundary condition 5 is satisfied.

The electrostatic energy $U_{\rm m}$ at fixed E_a is given by[9–12]

$$U_{\rm m} = \frac{1}{2}\sum_{\boldsymbol{m}} \left[\sum_{ij}{}' \frac{q_i q_j}{|\boldsymbol{r}_{ij} + \boldsymbol{h}|} - \sum_{ij} \frac{q_i q_j}{|\bar{\boldsymbol{r}}_{ij} + \boldsymbol{h}|}\right] - E_a M_z, \tag{8}$$

where $\boldsymbol{r}_{ij} = \boldsymbol{r}_i - \boldsymbol{r}_j$, $\bar{\boldsymbol{r}}_{ij} = \boldsymbol{r}_i - \bar{\boldsymbol{r}}_j$, and

$$M_z = \sum_i q_i z_i = \sum_k \mu_{zk} \tag{9}$$

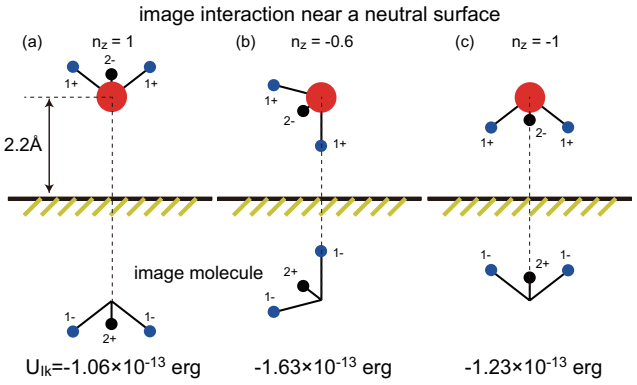

FIG. 1: Three typical configurations of a water molecule, whose oxygen atom is separated by 2.2Å from a metal wall without applied electric field. Image potential U_{Ik} in eq 13 is calculated to be (a) -1.06 ($n_z = 1$), (b) -1.63 ($n_z = -0.6$), and (c) -1.23 ($n_z = -1$) in units of 10^{-13}erg, where $n_z = \cos\theta$ with θ being the angle between the polarization direction and the z axis. H-down orientation (b) has the lowest electrostatic energy and most frequently appears close to the wall without applied electric field.

is the total polarization along the z axis. In $\sum'_{ij}$ in eq 8, we exclude the self term with $j = i$ for $\boldsymbol{h} = (0, 0, 0)$. For infinitesimal changes $\boldsymbol{r}_i \to \boldsymbol{r}_i + d\boldsymbol{r}_i$ and $E_a \to E_0 + dE_a$, the incremental change of $U_{\rm m}$ in eq 8 is of the following differential form,

$$dU_{\rm m} = -\sum_i q_i \boldsymbol{E}_i \cdot d\boldsymbol{r}_i - M_z dE_a, \tag{10}$$

where $\boldsymbol{E}_i = -q_i^{-1}\nabla_i U_{\rm m}$ is the local electric field acting on charge i at fixed $\Delta\Phi$. Hereafter, $\nabla_i = \partial/\partial \boldsymbol{r}_i$. The local electric field $\boldsymbol{E}_k$ on molecule k will be defined in Appendix A.

The first term in eq 8 is periodic in 3D with respect to $x_i \to x_i \pm L$, $y_i \to y_i \pm L$, and $z_i \to z_i \pm 2H$ due to the summation over $\boldsymbol{h}$. Thus, it can be calculated with the 3D Ewald method. So far, a few groups have performed simulations on the basis of $U_{\rm m}$ in eq 8.[9–12]. In the Ewald method, the Coulomb potential $q_i q_j/r$ is divided into the long-range part $q_i q_j \psi_\ell(r)$ and the short-range part $q_i q_j \psi_s(r)$ with

$$\psi_\ell(r) = {\rm erf}(\gamma r)/r, \quad \psi_s(r) = [1 - {\rm erf}(\gamma r)]/r. \tag{11}$$

where ${\rm erf}(u)$ is the error function and γ^{-1} represents the potential range of $\psi_s(r)$. It follows the Poisson equation $-\nabla^2\psi_\ell(r) = 4\pi\varphi_3(r)$ with $\varphi_3(r) = \varphi(x)\varphi(y)\varphi(z)$, where

$$\varphi(z) = (\gamma/\sqrt{\pi})\exp(-\gamma^2 z^2) \tag{12}$$

is the 1D Gaussian distribution with $\int dz\varphi(z) = 1$. In this paper, we set $\gamma = 0.85/\sigma = 2.7$ /nm.

It is well-known that the image interaction grows when a charge or a dipole approaches a wall. For a water molecule k near the bottom wall at $z = 0$, the image potential from the closest images grows in $U_{\rm m}$:

$$U_{Ik} = -\sum_{\alpha\neq\beta} \frac{q_\alpha q_\beta}{2|\boldsymbol{r}_{k\alpha} - \bar{\boldsymbol{r}}_{k\beta}|}, \tag{13}$$

where $\alpha, \beta = {\rm H1}, {\rm H2}, {\rm M}$. In Fig.1, typical molecular configurations are illustrated. At $z_{k\rm O} = 2.2$Å, the above U_{Ik} is lower for (b) than that for (a) by 5.7×10^{-14} erg ($= 1.4 k_B T$ for $T = 298$ K). Therefore, the image interaction favors the H down configuration (b) near a metal wall, though the molecular orientations near a wall are cooperative due to the hydrogen bonding (see Fig.5).

C. Surface Charges. The image charges are introduced as a mathematical convenience. The real charges are those in the cell and the surface charges (excess electrons) on the metal walls. The latter attract and orient dipoles near the walls. Here, we examine the effects of the latter in detail.

The surface charge densities are written as $\sigma_0(\boldsymbol{r}_\perp)$ at $z = 0$ and $\sigma_H(\boldsymbol{r}_\perp)$ at $z = H$, where $\boldsymbol{r}_\perp = (x, y)$. Since the charges in the cell are expelled from the walls due to the wall potentials, σ_0 and σ_H are expressed in terms of $E_z(x, y, z) = -\partial\Phi/\partial z$ as

$$\sigma_0 = E_z(x, y, 0)/4\pi, \quad \sigma_H = -E_z(x, y, H)/4\pi. \tag{14}$$

We consider their lateral mean surface charges,

$$\bar\sigma_0 = \frac{1}{L^2}\int dS\sigma_0(\boldsymbol{r}_\perp), \quad \bar\sigma_H = \frac{1}{L^2}\int dS\sigma_H(\boldsymbol{r}_\perp), \tag{15}$$

where $dS = dxdy$ and $0 < x, y < L$. From eq B4 in Appendix B, these mean values exactly satisfy[9,12]

$$\bar\sigma_0 = -\bar\sigma_H = E_a/4\pi + M_z/V. \tag{16}$$

We write the potential from the surface charges as Φ_s and divide it into two parts,

$$\Phi_s(\boldsymbol{r}) = -4\pi\bar\sigma_0 z + \phi_s(\boldsymbol{r}). \tag{17}$$

The first term arises from the mean surface charges. The second contribution ϕ_s is due to the surface charge deviations, which will be estimated in Sec.III.

In the 2D Fourier series, we set

$$\Delta\sigma_0(\boldsymbol{r}_\perp) = \sigma_0(\boldsymbol{r}_\perp) - \bar\sigma_0 = \sum_{\boldsymbol{k}\neq\boldsymbol{0}} \sigma_{0\boldsymbol{k}} e^{{\rm i}\boldsymbol{k}\cdot\boldsymbol{r}_\perp},$$
$$\Delta\sigma_H(\boldsymbol{r}_\perp) = \sigma_H(\boldsymbol{r}_\perp) - \bar\sigma_H = \sum_{\boldsymbol{k}\neq\boldsymbol{0}} \sigma_{H\boldsymbol{k}} e^{{\rm i}\boldsymbol{k}\cdot\boldsymbol{r}_\perp}, \tag{18}$$

where $\boldsymbol{k} = (2\pi/L)(n_x, n_y) \neq (0, 0)$ with n_x and n_y being integers. The Fourier components are calculated as[12]

$$\sigma_{0\boldsymbol{k}} = \frac{-1}{L^2}\sum_j q_j \frac{\sinh(kH - kz_j)}{\sinh(kH)} e^{-{\rm i}\boldsymbol{k}\cdot\boldsymbol{r}_j},$$
$$\sigma_{H\boldsymbol{k}} = \frac{-1}{L^2}\sum_j q_j \frac{\sinh(kz_j)}{\sinh(kH)} e^{-{\rm i}\boldsymbol{k}\cdot\boldsymbol{r}_j}, \tag{19}$$

where $k = |\boldsymbol{k}| \neq 0$ and the summation over m_z in eq 7 has been performed to give the hyperbolic sine functions. The potential deviation ϕ_s is expressed as

$$\phi_s = \sum_{\boldsymbol{m}_\perp} \int dS' \left[\frac{\Delta\sigma_0(\boldsymbol{r}_\perp')}{|\boldsymbol{r} - \boldsymbol{r}' + L\boldsymbol{m}_\perp|} + \frac{\Delta\sigma_H(\boldsymbol{r}_\perp')}{|\boldsymbol{r} - \boldsymbol{r}'' + L\boldsymbol{m}_\perp|} \right]$$
$$= \sum_{\boldsymbol{k}\neq\boldsymbol{0}} \frac{2\pi}{k} \left[\sigma_0 \boldsymbol{k} e^{-kz} + \sigma_H \boldsymbol{k} e^{k(z-H)} \right] e^{i\boldsymbol{k}\cdot\boldsymbol{r}_\perp}. \quad (20)$$

In the first line, $dS' = dx'dy'$, $\boldsymbol{r}_\perp' = (x', y')$, $\boldsymbol{r}' = (x', y', 0)$, $\boldsymbol{r}'' = (x', y', H)$, and $\boldsymbol{m}_\perp = (m_x, m_y, 0)$ with m_x and m_y being integers. The second line is the 2D Fourier expansion of the first line, where we use the 2D integral $\int dS e^{i\boldsymbol{k}\cdot\boldsymbol{r}_\perp}/r = 2\pi e^{-kz}/k$.

The total potential $\Phi(\boldsymbol{r})$ ($\boldsymbol{r} \neq \boldsymbol{r}_j$) in eq 6 arises from the charges in the cell and those on the walls as

$$\Phi = \sum_{\boldsymbol{m}_\perp} {\sum_j}' \frac{q_j}{|\boldsymbol{r} - \boldsymbol{r}_j + L\boldsymbol{m}_\perp|} + \phi_s(\boldsymbol{r}) - 4\pi\bar{\sigma}_0 z, \quad (21)$$

which also follows if we substitute eq 19 into the second line of eq 20. The summation over $\boldsymbol{m}_\perp$ in the first term ensures the lateral periodicity. From eq 9, $\phi_s(\boldsymbol{r})$ is also written in terms of the image potentials as

$$\phi_s = \sum_{\boldsymbol{m}} \sum_j \left[\frac{q_j(1-\delta_{m_z 0})}{|\boldsymbol{r} - \boldsymbol{r}_j + \boldsymbol{h}|} - \frac{q_j}{|\boldsymbol{r} - \bar{\boldsymbol{r}}_j + \boldsymbol{h}|} \right]$$
$$+4\pi M_z z/V, \quad (22)$$

where δ_{mn} is the Kronecker delta and $\boldsymbol{h}$ is expressed as eq 7. The first term in eq 22 is the sum of the image potentials. Far from the walls, we shall see that it is mostly canceled by the second term ($\propto M_z$), leading to small ϕ_s (see Sec.III).

Using eq 22, we rewrite the electrostatic energy $U_{\rm m}$ in eq 8 using ϕ_s as

$$U_{\rm m} = \frac{1}{2} \sum_{\boldsymbol{m}_\perp} {\sum_{i,j}}' \frac{q_i q_j}{|\boldsymbol{r}_i - \boldsymbol{r}_j + L\boldsymbol{m}_\perp|} + \sum_j \frac{q_j}{2} \phi_s(\boldsymbol{r}_j)$$
$$-2\pi M_z^2/V - E_a M_z, \quad (23)$$

The third term ($\propto M_z^2$) in eq 23 is a mean-field contribution, which is large in applied field. Using the relation $\nabla_i \sum_j q_j \phi_s(\boldsymbol{r}_j) = -2q_i \boldsymbol{E}_s(\boldsymbol{r}_i)$, the local field $\mathbf{E}_i$ in eq 10 is divided as

$$\boldsymbol{E}_i = \boldsymbol{E}_i^d + \boldsymbol{E}_s(\boldsymbol{r}_i) + 4\pi\bar{\sigma}_0 \boldsymbol{e}_z. \quad (24)$$

The $\boldsymbol{E}_i^d$ arises from the charges in the cell and $\boldsymbol{E}_s(\boldsymbol{r})$ from the surface charge deviations so that

$$\boldsymbol{E}_i^d = \sum_{\boldsymbol{m}_\perp} {\sum_j}' q_j \boldsymbol{g}(\boldsymbol{r}_i - \boldsymbol{r}_j + L\boldsymbol{m}_\perp), \quad (25)$$
$$\boldsymbol{E}_s(\boldsymbol{r}) = -\nabla\phi_s(\boldsymbol{r}). \quad (26)$$

where $\boldsymbol{g}(\boldsymbol{r}) = -\nabla r^{-1} = r^{-3}\boldsymbol{r}$. The third term in eq 24 arises from the mean surface charge, where $\boldsymbol{e}_z$ is the unit vector along the z axis. In Sec.IIIE, we will further divide $\boldsymbol{E}_i^d$ into long-range and short-range parts.

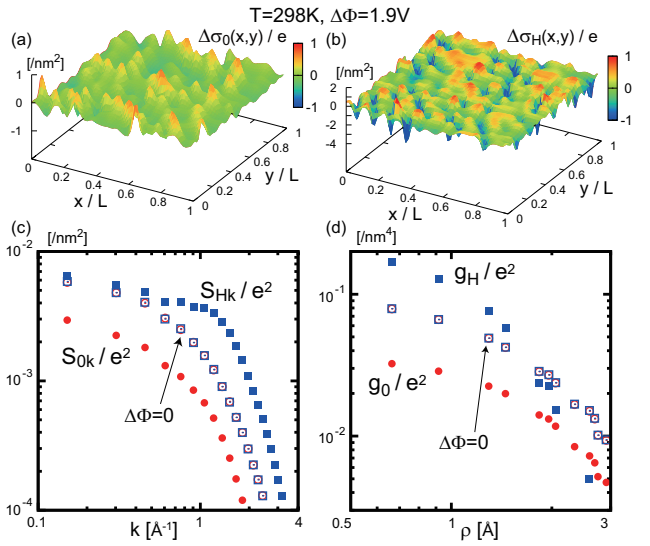

FIG. 2: Snapshots of surface charge deviations (a) $\Delta\sigma_0(x, y)$ at $z = 0$ and (b) $\Delta\sigma_H(x, y)$ at $z = H$ divided by e at $T =$ 298K, where $\Delta\Phi = 1.9$V ($E_a = 0.42$ V/nm). (c) Surface-charge structure factors S_{0k} and S_{Hk} in eq 27 vs k and (d) surface-charge spatial correlation functions $g_0(\rho)$ and $g_H(\rho)$ in eq 28 vs $\rho = (x^2 + y^2)^{1/2}$, where $\Delta\Phi = 0$ and 1.9 V. These quantities are divided by e^2.

Yeh and Berkowitz[13] used the 3D Ewald method with empty slabs under applied electric field. They replaced E_a by $E_a + 4\pi M_z/V$ in the equations of motion, so their method is justified by eqs 23 and 24 provided that ϕ_s is negligible far from the walls.

III. EQUILIBRIUM STATES UNDER ELECTRIC FIELD

We performed MD simulation using $U_{\rm m}$ in eq 8 with the 3D Ewald method. The molecule number is $N = 2400$ and the cell dimensions are $L = 41.5$Å and $H = 44.7$Å with volume $V = L^2H \cong 77\text{nm}^3$. The temperature is fixed at $T = 298$ K in the NVT ensemble with a Nosé-Hoover thermostat. See the beginning of Sec.IVA for remarks on the NVE simulation. In this section, the symbol $\langle\cdots\rangle$ denotes the time average over 6 ns, which is taken as the equilibrium average.

A. Effects of Surface Charges. In Fig.2, we present snapshots of (a) the surface charge deviations $\Delta\sigma_0(x, y)$ at $z = 0$ and (b) $\Delta\sigma_H(x, y)$ at $z = H$ with $\Delta\Phi = 1.9$ V or $E_a = 0.42$ V/nm, where the bottom (top) wall is positively (negatively) charged with $\bar{\sigma}_0/e = 0.44/\text{nm}^2$. Here, the fluctuation amplitude of $\Delta\sigma_H$ is larger than that of $\Delta\sigma_0$, because the protons can be closer to the top wall than the oxygen atoms to the bottom wall. In (c), we display the 2D structure factors S_{0k} and S_{Hk} for the

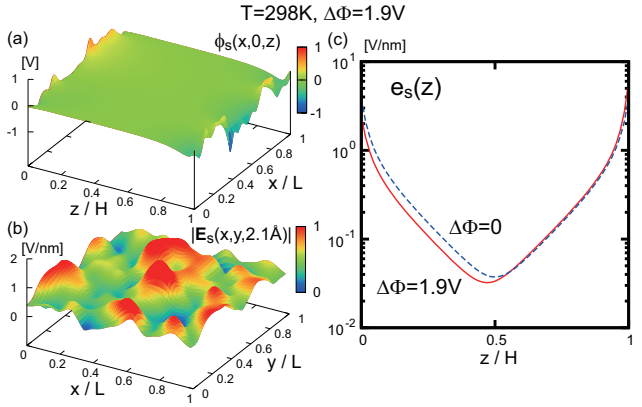

FIG. 3: Snapshots of (a) electric potential $\phi_s(x,0,z)$ due to the surface charge deviations at $y=0$ in the zx plane and (b) $|\boldsymbol{E}_s(x,y,z)| = |\nabla\phi_s|$ at $z = 2.1$Å in the xy plane, where $\Delta\Phi = 1.9$V ($E_a = 0.42$ V/nm) and $T = 298$K as in Fig.2. (c) Electric-field fluctuation amplitude $e_s(z)$ in eq 29.

thermal fluctuations of the surface charges defined by

$$S_{0k} = L^2\langle|\sigma_{0\boldsymbol{k}}|^2\rangle, \quad S_{Hk} = L^2\langle|\sigma_{H\boldsymbol{k}}|^2\rangle. \tag{27}$$

which depend only on $k = |\boldsymbol{k}|$ for $kL \gg 1$. Here, S_{Hk} is considerably larger than S_{0k} for $\Delta\Phi = 1.9$ V, while they coincide for $\Delta\Phi = 0$. Setting $S_{\lambda 0}/S_{\lambda k} = 1 + \xi_{s\lambda}^2 k^2 + \cdots$ for small k, we determine the correlation lengths ξ_{s0} and ξ_{sH}. Then, $\xi_{s0} = 1.95$ Å and $\xi_{sH} = 0.95$ Å $\sim 0.5\xi_{s0}$ for $\Delta\Phi = 1.9$ V, while $\xi_{s0} = \xi_{sH} = 1.6$ Å for $\Delta\Phi = 0$. In (d), we present the corresponding 2D pair correlation functions $g_0(\rho)$ and $g_H(\rho)$ expressed as

$$g_\lambda(\rho) = \langle\Delta\sigma_\lambda(\boldsymbol{0})\Delta\sigma_\lambda(\boldsymbol{r}_\perp)\rangle = \frac{1}{L^2}\sum_{\boldsymbol{k}\neq\boldsymbol{0}} S_{\lambda k} e^{i\boldsymbol{k}\cdot\boldsymbol{r}_\perp}, \tag{28}$$

where $\lambda = 0, H$, and $\boldsymbol{r}_\perp = (x,y)$, These functions depend only on $\rho = |\boldsymbol{r}_\perp| = (x^2+y^2)^{1/2}$ for $\rho \ll L$. Here, $g_0(0)/e^2 = \langle|\Delta\sigma_0|^2\rangle/e^2 = 0.037/\text{nm}^4$ and $g_H(0)/e^2 = \langle|\Delta\sigma_H|^2\rangle/e^2 = 0.224/\text{nm}^4$ for $\Delta\Phi = 1.9$ V in accord with the amplitude difference in (a) and (b), while these quantities are about $0.095/\text{nm}^4$ for $\Delta\Phi = 0$.

We are also interested in the electric field created by the surface charge deviations. In Fig.3, we show examples of cross-sectional snapshots of (a) $\phi_s(x,0,z)$ in the zx plane and (b) $|\boldsymbol{E}_s(x,y,2.1\text{ Å})|$ in the xy plane. Here, ϕ_s tends to zero far from the walls, while ϕ_s and $\boldsymbol{E}_s$ fluctuates near the walls. Using the second line of eq 20, we introduce the fluctuation amplitude $e_s(z)$ of $\boldsymbol{E}_s(\boldsymbol{r}) = -\nabla\phi_s(\boldsymbol{r})$ by

$$e_s(z)^2 = \langle|\boldsymbol{E}_s|^2\rangle = \frac{8\pi^2}{L^2}\sum_{\boldsymbol{k}\neq\boldsymbol{0}}\sum_{\lambda=0,H} S_{\lambda k} e^{-2k|z-\lambda|}. \tag{29}$$

where $e_s(z)$ depends only on z due to the averages in time and in the xy plane. In (c), we display $e_s(z)$ for $\Delta\Phi = 0$ and 1.9 V, which becomes very small away from the walls. In Appendix C, we will examine the behavior of $e_s(z)$ away from the walls in more detail.

B. Average 1D Polarization and Potential. In Appendix B, we will give the microscopic expression for the polarization density $\boldsymbol{p}(\boldsymbol{r})$ for water molecules. In our 1D geometry, the average polarization along the z axis is equal to the average in the xy plane:

$$P(z) = \langle p_z(\boldsymbol{r})\rangle = \frac{-1}{L^2}\sum_j \langle q_j\theta(z-z_j)\rangle, \tag{30}$$

where $\theta(u)$ is the step function being 0 for $u \le 0$ and 1 for $u > 0$. We may then define the average Poisson electric potential $\Psi(z)$ and field $\mathcal{E}(z) = -d\Psi/dz$ as[9,13,14]

$$\Psi(z) = -4\pi\langle\bar\sigma_0\rangle z + 4\pi\int_0^z dz' P(z'), \tag{31}$$

$$\mathcal{E}(z) = 4\pi\langle\bar\sigma_0\rangle - 4\pi P(z). \tag{32}$$

where $\langle\bar\sigma_0\rangle$ is the average of $\bar\sigma_0$. In our case, the temporal fluctuations of $\bar\sigma_0$ are very small and we need not distinguish between $\bar\sigma_0$ and $\langle\bar\sigma_0\rangle$. From eqs 30 and 31, $\Psi(z)$ satisfies $\Psi(0) = 0$, $\Psi(H) = -E_aH$, and

$$\frac{d^2\Psi(z)}{dx^2} = 4\pi\frac{dP(z)}{dz} = -\frac{4\pi}{L^2}\sum_j\langle q_j\delta(z-z_j)\rangle. \tag{33}$$

Taking the average of eq 16 gives

$$\langle\bar\sigma_0\rangle = -\langle\bar\sigma_H\rangle = E_a/4\pi + \int_0^H dz P(z)/H, \tag{34}$$

where $\int_0^H dz P(z) = \langle M_z\rangle/L^2$. The $P(z)$, $\Psi(z)$, and $\mathcal{E}(z)$ correspond to the polarization, electric potential, and electric field in the continuum electrostatics. The effective dielectric constant of a film may be defined in terms of $\langle\bar\sigma_0\rangle$ or $\langle M_z\rangle$ as[9,14]

$$\varepsilon_{\text{eff}} = 4\pi\langle\bar\sigma_0\rangle/E_a = 1 + 4\pi\langle M_z\rangle/VE_a. \tag{35}$$

In addition, U_{m} in eq 8 or eq 23 yields $\langle M_z\rangle = \langle M_z^2\rangle_0 E_a/k_BT$ in the limit of small E_a, where $\langle\cdots\rangle_0$ is the equilibrium average with $\Delta\Phi = 0$. Thus, $\langle M_z\rangle_0 = 0$. The linear response expression for ε_{eff} is given by[31,33,37,38]

$$\lim_{\Delta\Phi\to 0}\varepsilon_{\text{eff}} = 1 + 4\pi\langle M_z^2\rangle_0/Vk_BT. \tag{36}$$

In Fig.4, (a) $4\pi P(z)$ and (b) $\Psi(z)$ are displayed for $\Delta\Phi = 0$ and 1.9 V. Here, there appear Stern boundary layers[22,23] near the walls. Its thickness is given by $d = 4.7$Å if it is defined as the first maximum distance of $\Psi(z)$ for $\Delta\Phi = 0$. Even for $\Delta\Phi = 1.9$ V, the layer thickness is of this order, while $\Psi(z)$ becomes oscillatory near the walls. Outside the layers ($z > d$ and $H - z > d$), a homogeneous (bulk) state is realized with thickness $H - 2d(= 3.5$ nm here$)$[9,12–14], where $P(z)$ and $\mathcal{E}(z)$ are constant as

$$P(z) \cong P_b, \quad \mathcal{E}(z) \cong E_b = 4\pi(\langle\bar\sigma_0\rangle - P_b). \tag{37}$$

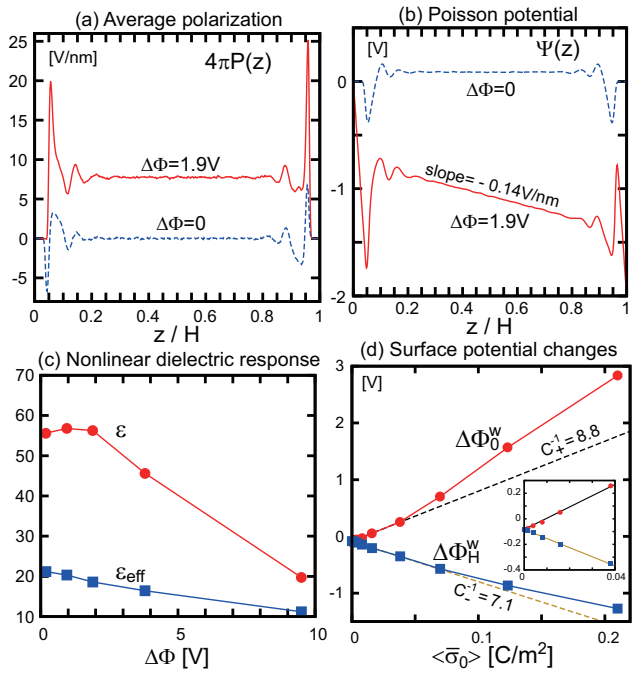

FIG. 4: Average 1D profiles at $T = 298$ K. (a) $4\pi P(z)$ in eq 30 and (b) $\Psi(z)$ in eq 31 for $\Delta\Phi = 0$ and 1.9 V. (c) $\varepsilon_{\rm eff}$ in eq 35 and ε in eq 38 vs $\Delta\Phi$. (d) $\Delta\Phi_0^{\rm w}$ and $\Delta\Phi_H^{\rm w}$ in eq 40 vs $\langle\bar\sigma_0\rangle$. In the inset, small-field behavior is expanded, indicating the zero-field limit $\Phi_{00}^{\rm w} \cong -0.09$ V in eq 44.

The P_b and E_b are the bulk polarization and electric field, respectively. The bulk dielectric constant is given by[13]

$$\varepsilon = 4\pi\langle\bar\sigma_0\rangle/E_b = 1 + 4\pi P_b/E_b. \tag{38}$$

In Fig.4(c), we show $\varepsilon_{\rm eff}$ and ε vs $\Delta\Phi$, where they exhibit considerable nonlinear behavior with increasing $\Delta\Phi$. We find $\varepsilon \sim 60$ for small $\Delta\Phi$ as in the previous simulations[8,13,14,38]. However, as $\Delta\Phi \to 0$, E_b becomes very small and ε cannot be determined precisely from eq 38. As regards $\varepsilon_{\rm eff}$, the right hand side of the linear response formula (36) is calculated to be 21.4, which coincides with $\varepsilon_{\rm eff}$ from eq 35 at small $\Delta\Phi$ in (c). In the three regions $z < d$ (bottom), $0.3 < z/H < 0.7$ (bulk), and $H - z < d$ (top), the average of the z component n_{zk} is given by $0.02, 0$, and -0.02 for $\Delta\Phi = 0$ and by $0.35, 0.27$, and 0.33 for $\Delta\Phi = 1.9$ V, respectively. The dipoles are more aligned in the Stern layers than in the bulk with small asymmetry between bottom and top. The alignment tends to saturate with increasing $\Delta\Phi$. The average density in the bulk region is 33.97 nm^{-3} = 1.016 g/cm^3 for $\Delta\Phi = 0$ and 33.56 nm^{-3} = 1.004 g/cm^3 for $\Delta\Phi = 1.9$ V.

In the bulk, $\Psi(z)$ behaves linearly as

$$\Psi(z) \cong -E_b z - A_0, \tag{39}$$

where A_0 is a constant. We determine the excess potential changes in the Stern layers at $z = 0$ and H as[9,14]

$$\Delta\Phi_0^{\rm w} = \Psi(0) - \Psi(d) - E_b d,$$

TABLE I: **Data for water in equilibrium under electric field.** For $\Delta\Phi = 0.19$ V and 1.9 V at $T = 298$ K, listed are E_a (V/nm), E_b (V/nm), $4\pi P_b$ (V/nm), $4\pi\langle\bar\sigma_0\rangle$ (V/nm), $\varepsilon_{\rm eff}$, ε, $\Delta\Phi_0^{\rm w}$ (V), and $\Delta\Phi_H^{\rm w}$ (V). These are defined in eqs 35-40, while $\gamma_{\rm loc}$ is the Lorentz factor in bulk in eq 49. Instead of $4\pi\langle\bar\sigma_0\rangle$ in V/nm, we also have $\langle\bar\sigma_0\rangle/e = 0.05$ and 0.44, respectively, in nm^{-2}.

$\Delta\Phi$	E_a	E_b	$4\pi P_b$	$4\pi\langle\bar\sigma_0\rangle$	$\varepsilon_{\rm eff}$	ε	$\Delta\Phi_0^{\rm w}$	$\Delta\Phi_H^{\rm w}$	$\gamma_{\rm loc}$
0.19	0.042	0.016	0.88	0.90	21	56	-0.026	-0.14	0.58
1.9	0.42	0.14	7.7	7.9	19	56	0.70	-0.57	0.59

$$\Delta\Phi_H^{\rm w} = \Psi(H) - \Psi(H-d) + E_b d. \tag{40}$$

Then, $A_0 = \Delta\Phi_0^{\rm w}$ in eq 39. Use of $P(z)$ gives

$$\Delta\Phi_\lambda^{\rm w} = 4\pi \int_\lambda^{|\lambda-d|} dz[P_b - P(z)], \tag{41}$$

where $\lambda = 0, H$. Since $E_a H = \Phi_0 - \Phi_H = \Delta\Phi_0^{\rm w} - \Delta\Phi_H^{\rm w} + E_b H$, we define a surface electric length by

$$\ell_{\rm w} = (\Delta\Phi_0^{\rm w} - \Delta\Phi_H^{\rm w})/E_b. \tag{42}$$

The potential drop in the bottom and top layers is given by $\Delta\Phi\ell_{\rm w}/(\ell_{\rm w}+H)$. In terms of the ratio $\ell_{\rm w}/H$, the bulk quantities ε, E_b, and P_b can be related to the corresponding film quantities $\varepsilon_{\rm eff}$, E_a, and $\langle M_z\rangle/V$ as

$$\varepsilon/\varepsilon_{\rm eff} = E_a/E_b = 1 + \ell_{\rm w}/H, \tag{43}$$
$$P_b = \langle M_z\rangle/V + E_b\ell_{\rm w}/4\pi H. \tag{44}$$

In Fig.4(b), there arises a surface potential change even for $\Delta\Phi = 0$. We define the zero-field surface potential drop as

$$\Phi_{00}^{\rm w} = \lim_{\Delta\Phi\to 0}\Delta\Psi_0^{\rm w} = \lim_{\Delta\Phi\to 0}\Delta\Psi_H^{\rm w}. \tag{45}$$

For $\Delta\Phi \geq 0$ or for $\langle\bar\sigma_0\rangle \geq 0$, we relate $\Delta\Phi_0^{\rm w}$ and $\Delta\Phi_H^{\rm w}$ to $\langle\bar\sigma_0\rangle$ and $\langle\bar\sigma_H\rangle = -\langle\bar\sigma_0\rangle$ as

$$\Delta\Phi_0^{\rm w} = \Phi_{00}^{\rm w} + C_+^{-1}\langle\bar\sigma_0\rangle,$$
$$\Delta\Phi_H^{\rm w} = \Phi_{00}^{\rm w} + C_-^{-1}\langle\bar\sigma_H\rangle, \tag{46}$$

where C_+ and C_- are the surface capacitance[22,23] for positive and negative surface charges, respectively. From eqs 42 and 46 with the aid of eq 38, we obtain

$$\ell_{\rm w} = (C_+^{-1} + C_-^{-1})\varepsilon/4\pi. \tag{47}$$

In Table 1, we give examples of numerical values of E_b, $4\pi P_b$, $4\pi\langle\bar\sigma_0\rangle$, $\varepsilon_{\rm eff}$, ε, $\Delta\Phi_0^{\rm w}$, $\Delta\Phi_H^{\rm w}$, and $\gamma_{\rm loc}$ (see eq 49) for $\gamma_{\rm loc}$), setting $\Delta\Phi = 0.19$ and 1.9 V (E_a = 0.042 and 0.42 V/nm) at 298 K. In Fig.4(d),we have $\Phi_{00}^{\rm w} = -0.46(\epsilon/\sigma)^{1/2} = -0.019e/\sigma = -0.09$V. We also have the surface capacitance $C_+ = 1.0$/nm and $C_- = 1.4$/nm for $\langle\bar\sigma_0\rangle < 0.04$ C/m^2 = $0.24e$/nm^2 or for $\Delta\Phi < 1$ V, but they exhibit considerable nonlinear behavior for larger $\langle\bar\sigma_0\rangle$. In the usual units, they are written as $C_+ = 11\mu$F/cm^2, and $C_- = 14\mu$F/cm^2 for

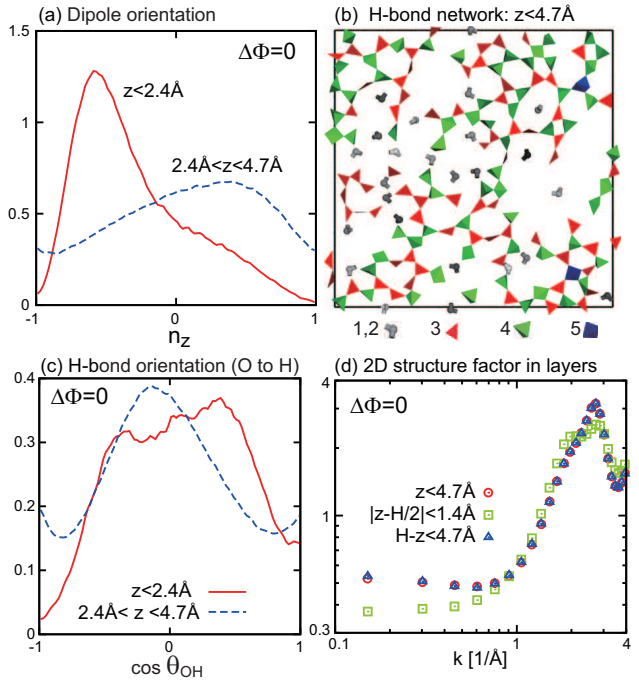

FIG. 5: (a) Distributions of the z component of the polarization direction n_{zk} in the first ($z < 2.4$ Å) and second (2.4 Å $< z <$ 4.7 Å) layers. (b) Snapshot of 167 molecules in the bottom Stern layer with intermolecular hydrogen bonds, whose numbers are 1, 2, 3, 4, and 5 as indicated below the panel. (c) Distributions of $\cos\theta_{k\mathrm{OH}}$ indicating planar alignment, where $\theta_{k\mathrm{OH}}$ is the intermolecular hydrogen bond angle with respect to the z axis (from O to H). (d) 2D structure factors of the molecular positions $(x_{k\mathrm{G}}, y_{k\mathrm{G}})$ in three layer regions $z < 4.7$ Å, $|z - H/2| < 1.4$ Å, and $H - z < 4.7$ Å, indicating planar mesoscopic fluctuations near the walls.

small $\langle\bar{\sigma}_0\rangle$. Thus, from eq 47, we find $\ell_{\mathrm{w}} = 8$ nm $\sim 2H$ for small $\langle\bar{\sigma}_0\rangle$, which is very long. As a result, we have $E_a/E_b = \varepsilon/\varepsilon_{\mathrm{eff}} \sim 3$ for our small system. In contrast, in our recent paper[12], we applied electric field to point dipoles interacting with the soft-core potential to obtain $\ell_{\mathrm{w}} \sim 2\sigma \sim 0.1H$ and $\varepsilon_{\mathrm{eff}} \cong \varepsilon$.

Hautman *et al.*[9] obtained $C_+ = 12.4\ \mu F/\mathrm{cm}^2$ and $C_- = 10.5\ \mu F/\mathrm{cm}^2$ using the SPC model, where $\varepsilon_{\mathrm{eff}}$ in eq 35 was 12 in one example in accord with eq 43. Yeh and Berkowitz[8,13] obtained $\varepsilon \sim 60$ for small $\Delta\Phi$. Willard *et al.*[14] obtained $\varepsilon \sim 75.07$, 61.50, and 57.30 for $\Delta\Phi$ =0.27, 1.36 and 2.72 V, respectively, together with $C_+ = 5.20\ \mu F/\mathrm{cm}^2$ and $C_- = 8.39\ \mu F/\mathrm{cm}^2$ using the SPC/E model. We may estimate ℓ_{w} in eq 47 using their data[9,14] to find $\ell_{\mathrm{w}} \sim 10$ nm as in our case. These numerical values of the surface capacitance are considerably smaller than the experimental values for electrolytes in contact with a metal surface[9,14,22,23].

For $\Delta\Phi = 0$, we may treat the Stern layer as a bilayer composed of two parts, $z < d_1$ =2.4 Å and $d_1 < z < d$ =4.7 Å, at the bottom. Here, $\Psi(z)$ in eq 31 takes a minimum at $z = d_1$ and a maximum at $z = d$ in Fig.4(b). In the first and second layers, the average areal density of water molecules and the average of $n_{zk} = \mu_{zk}/\mu_0$ are given by (1.6 nm^{-2}, -0.26) and (8.2 nm^{-2}, 0.073), respectively. See Fig.5(a), where displayed are the normalized distributions of n_{zk} in the two layers. The polarization is downward in the first layer and upward in the second. We remark that the zero-field potential drop is expressed as $\Phi_{00}^{\mathrm{w}} = -4\pi \int_0^d dz P(z)$ for $P_b = 0$ from eq 41. In our case, the integral of $P(z)/\mu_0$ in the first layer is $1.6 \times (-0.26) = -0.42$ nm^{-2} and that in the second layer is $8.2 \times 0.073 = 0.60$ nm^{-2}. As a result, we obtain $\Phi_{00}^{\mathrm{w}} = -0.09$ V. However, with increasing the water adsorption, the first layer contribution increases, leading to positive Φ_{00}^{w}. In fact, if we increased the coefficient C_3 of the attractive part of the wall potential in eq 4 by 10 times (with the other parameters unchanged), we obtained $\Phi_{00}^{\mathrm{w}} = 0.2$ V. Previously, Willard *et al.*[14] found $\Phi_{00}^{\mathrm{w}} \sim 0.8$ V for strong adsorption.

C. Hydrogen bonds. We also examine the intermolecular hydrogen bonds, which have been defined in various manners[39–42]. We treat two molecules to be hydrogen-bonded if one of the intermolecular OH distances is shorter than 2.4 Å and the angle between the OO vector and one of their intramolecular OH bonds is smaller than $\pi/6$. A similar definition was used by Zielkiewicz[40]. We here consider the hydrogen-bond number m_k from O and H atoms of molecule k and the hydrogen-bond angle $\theta_{k\mathrm{OH}} = \cos^{-1}(Z_{k\mathrm{OH}}/|\boldsymbol{R}_{k\mathrm{OH}}|)$ with respect to the z axis, where $\boldsymbol{R}_{k\mathrm{OH}}$ is the OH bond vector (with $Z_{k\mathrm{OH}}$ being its z component) from O of molecule k to H of another molecule.

In Fig.5(b), we display a snapshot of the 2D molecular positions $(x_{k\mathrm{G}}, y_{k\mathrm{G}})$ and the associated intermolecular hydrogen bonds with $1 \le m_k \le 5$ in the bottom Stern layer for $\Delta\Phi = 0$. The average of m_k is 3.2 here[34], which is smaller than their bulk average 3.6. We can see marked heterogeneous clustering of the hydrogen bonds. In particular, in blank regions, the molecules are collectively lifted by about 1 Å due to the hydrogen bonding near the wall. These molecular configurations evolve on a timescale of 1 ps[35]. In Fig.5(c), we examine the equilibrium distribution of $\cos\theta_{k\mathrm{OH}}$ at the bottom for $\Delta\Phi = 0$, which is maximized at angle $1.1\pi/2$ for the first layer and $0.73\pi/2$ for the second. As was reported previously[14,34,35], the intermolecular hydrogen bonds near a wall tend to make relatively small angles with respect to the wall plane. In Fig.5(d), we present the 2D structure factors of the molecular positions for $\Delta\Phi = 0$ in the three regions given by $z < d$, $|z - H/2| < 1.4$ Å, and $H - z < d$. For small $k < 1$ Å^{-1}, density fluctuations are enhanced appreciably near the walls, but enhancement is not detectable in the middle.

Bratko *et al.*[43] applied electric field to water in the directions parallel and perpendicular to hydrocarbon-like walls. They found that electrostriction and surface affinity (relevant to electrowetting) were more pronounced for parallel field than for perpendicular field as a result of hydrogen bond optimization.

D. Local Electric Field. In Appendix A, we will define the local electric field $\boldsymbol{E}_k^{\rm loc}$ acting on each molecule k as a linear combination of $\boldsymbol{E}_{k\alpha}$ ($\alpha = {\rm H1}, {\rm H2}, {\rm M}$) at the constituting charged points. For the TIP4P/2005 model, it is expressed as

$$\boldsymbol{E}_k^{\rm loc} = \frac{1}{2}(1+b_{\rm M})(\boldsymbol{E}_{k{\rm H1}} + \boldsymbol{E}_{k{\rm H2}}) - b_{\rm M}\boldsymbol{E}_{k{\rm M}}, \tag{48}$$

where $b_{\rm M} = 0.208$. If we write $\boldsymbol{E}_k^{\rm loc} = \sum_\alpha A_\alpha \boldsymbol{E}_{k\alpha}$, we have $A_{\rm H1} = A_{\rm H2} = (1+b_{\rm M})/2$ and $A_{\rm M} = -b_{\rm M}$. Using eq 48, we calculated the average of its z component $E_{\rm loc} = \langle E_{zk}^{\rm loc}\rangle_b$. We also calculated the bulk average field E_b and polarization P_b in eq 37. They are related as

$$E_{\rm loc} = \langle E_{zk}^{\rm loc}\rangle_b = E_b + 4\pi\gamma_{\rm loc}P_b, \tag{49}$$

which is the definition of the Lorentz factor $\gamma_{\rm loc}$. In our simulation, we find $\gamma_{\rm loc} \cong 0.58$ for all $\Delta\Phi$ investigated (see Table 1 for $\Delta\Phi = 0.19$ and 1.9 V). Hereafter, $\langle\cdots\rangle_b$ denotes the averages over molecules in the region $0.3H < z_{k\rm G} < 0.7H$ and over a time interval of 6 ns, where $z_{k\rm G}$ is the z component of the center of mass of molecule k.

We further consider the equilibrium distribution of the z component $E_{zk}^{\rm loc}$ in the bulk defined by

$$P_{\rm loc}(E) = \langle\delta(E_{zk}^{\rm loc} - E)\rangle_b, \tag{50}$$

In Fig.6(a), the distribution $P_{\rm loc}(E)$ of the local field along the z axis is non-Gaussian with broad width about 15 V/ nm. To understand this width, we note that a charge e separated by $\sigma(\cong 3.2$ Å) creates an electric field with size $e/\sigma^2 \cong 14$ V/nm. The mean value is written as $E_{\rm loc} = \langle E_{zk}^{\rm loc}\rangle_b = \int dE P_{\rm loc}(E)E$. where $E_{\rm loc} = 0.53$ and 4.7 V/nm for $\Delta\Phi = 0.19$ and 1.9 V, respectively.

The distributions of electric field fluctuations have been calculated in water and electrolytes (for $\Delta\Phi = 0$)[44–46]. In particular, Sellner *et al.*[46] have obtained those at O and H sites, which resemble to $P_{\rm loc}^z(E)$ for $\Delta\Phi = 0$ in Fig.6(a). We remark that the effect of molecular stretching in strong local field should be examined[32,33].

E. Continuum Electrostatics. Next, for each molecule k in the region $0.3H < z_{k\rm G} < 0.7H$, we consider a sphere with radius $R = 4\sigma = 12.6$ Å around the center of mass $\boldsymbol{r}_{k\rm G}$. We then divide $\boldsymbol{E}_k^{\rm loc}$ as

$$\boldsymbol{E}_k^{\rm loc} = \boldsymbol{E}_k^{\rm in} + \boldsymbol{E}_k^{\rm out}, \tag{51}$$

where the first term is the contribution from molecules ℓ inside the sphere ($|\boldsymbol{r}_{\ell\rm G} - \boldsymbol{r}_{k\rm G})| < R$) and the second term is that from those outside it and the surface (or image) charges. Using the step function $\theta(u)$, we write $\boldsymbol{E}_k^{\rm in}$ as

$$\boldsymbol{E}_k^{\rm in} = \sum_{\ell\neq k,\alpha,\beta} \theta(R - |\boldsymbol{r}_{\ell\rm G} - \boldsymbol{r}_{k\rm G})|)A_\alpha q_\beta \boldsymbol{g}(\boldsymbol{r}_i - \boldsymbol{r}_j), \tag{52}$$

where $i = k\alpha$, $j = \ell\beta$ with $\ell \neq k$ and $\alpha, \beta =$ H1, H2, M, and $\boldsymbol{g}(\boldsymbol{r}) = r^{-3}\boldsymbol{r}$. The coefficients A_α appear below eq 48.

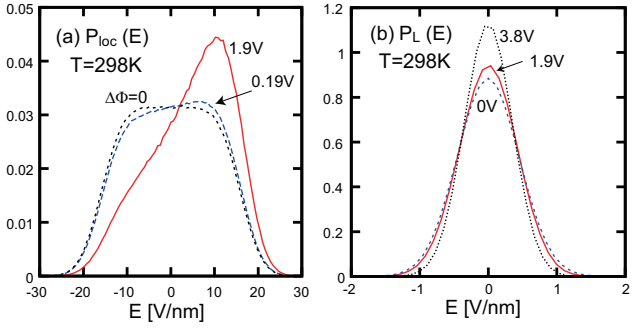

FIG. 6: (a) Distribution $P_{\rm loc}(E)$ of local field $E_{zk}^{\rm loc}$ in eq 50 for $\Delta\Phi = 0$, 0.19, and 1.9 V ($E_a = 0$, 0.042, and 0.42 V/nm). (b) Distribution $P_{\rm L}(E)$ of deviation $F_{zk}^{\rm loc}$ in eq 54 for $\Delta\Phi = 0$, 1.9, and 3.8 V ($E_a = 0$, 0.42, and 0.84 V/nm), which is Gaussian with narrow width.

In the continuum electrostatics[24], $\boldsymbol{E}_k^{\rm out}$ is given by the classical value $E_b + 4\pi P_b/3 = [(\varepsilon+2)/3]E_b$ along the z axis in the 1D geometry. This approximation should become increasingly accurate with increasing R. Thus, we consider the deviation of $\boldsymbol{E}_k^{\rm out}$ from its continuum limit, which is written as

$$\boldsymbol{F}_k^{\rm loc} = \boldsymbol{E}_k^{\rm out} - (E_b + 4\pi P_b/3)\boldsymbol{e}_z. \tag{53}$$

We calculated the equilibrium distribution of its z component $F_{zk}^{\rm loc}$ in the bulk:

$$P_{\rm L}(E) = \langle\delta(F_{zk}^{\rm loc} - E)\rangle_b. \tag{54}$$

In Fig.6(b), $P_{\rm L}(E)$ is excellently Gaussian: $P_{\rm L}(E) \cong \exp(-E^2/2s_{\rm L})/\sqrt{2\pi s_{\rm L}}$, where $\sqrt{s_{\rm L}} = 0.45$, 0.42, and 0.35 V/nm for $\Delta\Phi = 0$, 1.9, and 3.8 V, respectively. The mean value from $P_{\rm L}(E)$ vanishes, so $F_{\rm loc} = \langle F_{zk}^{\rm loc}\rangle_b \cong 0$. See Fig.7(b) also, where $F_{\rm loc} \cong 0$ for any $\Delta\Phi$ investigated. Since $E_{\rm loc} = \langle E_{zk}^{\rm loc}\rangle = \langle E_{zk}^{\rm in}\rangle + E_b + 4\pi P_b/3$ from eq 51, the Lorentz factor $\gamma_{\rm loc}$ in eq 49 is expressed as

$$\gamma_{\rm loc} = 1/3 + E_{\rm in}/4\pi P_b. \tag{55}$$

where $E_{\rm in} = \langle E_{zk}^{\rm in}\rangle_b$. Thus, the deviation of $\gamma_{\rm loc}$ from the classical value 1/3 arises from the molecules inside the sphere. Our calculation of $E_{\rm loc}$ gives $E_{\rm in} \cong 0.25 \times 4\pi P_b$. Therefore, the internal field fluctuations ($\sim e/\sigma^2$) are due to the contribution $\boldsymbol{E}_k^{\rm in}$ from the molecules within the sphere. As a result, the distribution of $\boldsymbol{E}_k^{\rm in}$ is nearly equal to that of $\boldsymbol{E}_k^{\rm loc} - (E_b + 4\pi P_b/3)\boldsymbol{e}_z$. in the bulk. We confirmed that the distribution of its z component $\langle\delta(E_{zk}^{\rm in} - E)\rangle_b$ is equal to $P_L(E + E_b + 4\pi P_b/3)$ (see Fig.6(a)).

The above results indicate that the continuum electrostatics can provide an accurate approximation for the electric field $\boldsymbol{E}_k^{\rm out}$ from dipoles and charges outside a nanometer-size sphere for each molecule k in the bulk. We should further check this aspect with varying R and for other geometries.

F. Average Electric Fields vs $\Delta\Phi$. We also examine long-range and short-range parts of the dipolar

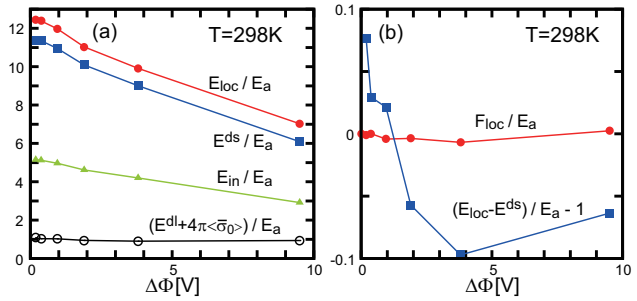

FIG. 7: Average fields along the z axis divided by E_a vs $\Delta\Phi$ in bulk. In (a), displayed are $E_{\rm loc} = \langle E^{\rm loc}_{zk}\rangle_b$, $E_{\rm in} = \langle E^{\rm in}_{zk}\rangle_b$, $E^{d\ell} + 4\pi\langle\bar\sigma_0\rangle = \langle E^{d\ell}_{zk}\rangle_b + 4\pi\langle\bar\sigma_0\rangle$, and $E^{ds} = \langle E^{ds}_{zk}\rangle_b$. In (b), combinations $F_{\rm loc} = \langle F^{\rm loc}_{zk}\rangle_b = (E_{\rm loc} - E_{\rm in}) - (E_b + 4\pi P_b/3)$ and $E_{\rm loc} - E^{ds} - E_a$ are shown to be small.

field $\boldsymbol{E}^d_i$ on charge i in eq 25 using the potential division $1/r = \psi_\ell(r) + \psi_s(r)$ in eq 11. Setting $\boldsymbol{g}_\ell(\boldsymbol{r}) = -\nabla\psi_\ell(r)$ and $\boldsymbol{g}_s(\boldsymbol{r}) = -\nabla\psi_s(r)$, we express these two parts as

$$\boldsymbol{E}^{d\ell}_i = \sum_{\boldsymbol{m}_\perp}\sum_j q_j \boldsymbol{g}_\ell(\boldsymbol{r}_i - \boldsymbol{r}_j + L\boldsymbol{m}_\perp), \tag{56}$$

$$\boldsymbol{E}^{ds}_i = \sum_{\boldsymbol{m}_\perp}{\sum_j}' q_j \boldsymbol{g}_s(\boldsymbol{r}_i - \boldsymbol{r}_j + L\boldsymbol{m}_\perp). \tag{57}$$

Then, $\boldsymbol{E}^d_i = \boldsymbol{E}^{d\ell}_i + \boldsymbol{E}^{ds}_i$. Notice that the self terms ($j = i$ for $\boldsymbol{m}_\perp = \boldsymbol{0}$) can be included in the long-range part in eq 56, because $\boldsymbol{g}_\ell(\boldsymbol{0}) = \boldsymbol{0}$ from $\psi_\ell(r) = (2\gamma/\sqrt{\pi})(1 - \gamma^2 r^2/3 + \cdots)$ for small r. Thus, we may rewrite $\boldsymbol{E}^{d\ell}_i$ as

$$\boldsymbol{E}^{d\ell}_i = \sum_{\boldsymbol{m}_\perp}\int d\boldsymbol{r}'\rho(\boldsymbol{r}')\boldsymbol{g}_\ell(\boldsymbol{r}_i - \boldsymbol{r}' + L\boldsymbol{m}_\perp), \tag{58}$$

where $\rho(\boldsymbol{r}) = \sum_j q_j\delta(\boldsymbol{r} - \boldsymbol{r}_j)$ is the charge density in the cell. These two parts contribute to the local field $\boldsymbol{E}^{\rm loc}_k$ in eq 48 as $\boldsymbol{E}^{d\ell}_k = \sum_\alpha A_\alpha \boldsymbol{E}^{d\ell}_{k\alpha}$ and $\boldsymbol{E}^{ds}_k = \sum_\alpha A_\alpha \boldsymbol{E}^{ds}_{k\alpha}$.

To estimate the long-range part $\boldsymbol{E}^{d\ell}_i$, we consider its continuum limit $\boldsymbol{E}^d_{\rm con}(\boldsymbol{r}_i)$. The latter is obtained if we replace $\rho(\boldsymbol{r})$ by $P_b[\delta(z - H + d) - \delta(z - d)]$ in eq 58, since the polarization is given by $P_b\boldsymbol{e}_z$ outside the Stern layers with thickness d in the continuum description. Then, the space integral $\int d\boldsymbol{r}'$ is performed to give

$$\boldsymbol{E}^d_{\rm con}(\boldsymbol{r}) = -4\pi P_b\boldsymbol{e}_z = (E_b - 4\pi\langle\bar\sigma_0\rangle)\boldsymbol{e}_z, \tag{59}$$

where $z \gg d$ and $H - z \gg d$. We numerically checked that $\boldsymbol{E}^{d\ell}_i$ is in fact close to $\boldsymbol{E}^d_{\rm con}$ in eq 59 for i in the bulk. This means that the molecules near the walls give rise to a dominant contribution to $\boldsymbol{E}^{d\ell}_i$. It follows that the sum of the averages $\langle E^{d\ell}_{zk}\rangle_b + 4\pi\langle\bar\sigma_0\rangle$ is of order $E_b \sim E_a$. In eq 24, we notice that the last term $4\pi\bar\sigma_0\boldsymbol{e}_z$ is largely canceled by the long-range part of the first term $\boldsymbol{E}^d_i$.

In Fig.7, we show the bulk averages of the z components of $\boldsymbol{E}^{\rm loc}_k$, $\boldsymbol{E}^{\rm in}_k$, $\boldsymbol{E}^{d\ell}_k$, and $\boldsymbol{E}^{ds}_k$ (divided by E_a) as functions of $\Delta\Phi$. In (a), $E_{\rm loc} = \langle E^{\rm loc}_{zk}\rangle_b$ and $E^{ds} = \langle E^{ds}_{zk}\rangle_b$ are of order $10E_a$. In accord with the discussion below eq 59, we can see the following relations,

$$E^{d\ell} = \langle E^{d\ell}_{zk}\rangle_b \cong -4\pi\langle\bar\sigma_0\rangle + E_a, \tag{60}$$

$$E^{ds} = \langle E^{ds}_{zk}\rangle_b \cong E_{\rm loc} - E_a, \tag{61}$$

which are consistent with eq 24 if $\boldsymbol{E}_s$ is neglected. Furthermore, in (b), $F_{\rm loc} = \langle F^{\rm loc}_{zk}\rangle_b = (E_{\rm loc} - E_{\rm in}) - (E_b + 4\pi P_b/3)$ is almost zero for any $\Delta\Phi$ in accord with Fig.6(b), while $E_{\rm loc} - E^{ds} - E_a = E^{d\ell} + 4\pi\langle\bar\sigma_0\rangle - E_a$ is at most 10% of E_a supporting the discussion below eq 59.

IV. FIELD REVERSAL

A. Situation and Method. In this section, we examine the relaxation after field reversal at $T = 298$ K in the NVT ensemble to avoid heating. For simplicity, the applied potential difference $\Delta\Phi$ (field E_a) is changed instantaneously from -1.9 V (-0.42 V/nm) to 1.9 V (0.42 V/nm) at $t = 0$. The system was in equilibrium for $t < 0$ and transient behaviors follow for $t > 0$. The polarization $M_z(t)$ changes continuously from $M_z(0) < 0$ to $M_z(\infty) = -M_z(0)$. From the last term in eq 23, the electrostatic energy $U_{\rm m}$ decreases by $2E_a|M_z(0)|$ after the field reversal. In this paper, we thus present the results in the NVT ensemble to suppress heating. If we used the NVE ensemble, we found heating by $\Delta T = 10 - 15$ K, where the kinetic energy increase given by $3k_B\Delta T$ per molecule was about one third of $2E_a|M_z(0)|/N$. However, these two simulations yielded essentially the same microscopic reorientation dynamics.

As an example, in Fig.8, we write one molecule at the center of each panel, which is undergoing a large angle change. The other molecules depicted are those which have been connected to the center molecule by hydrogen-bonding at some t in the time range 0.45 ps $\le t \le$ 0.72 ps. These surrounding molecules are also rotating in complex manners. In this section, we use the definition of hydrogen bonds given in Sec.IIIC. In the literature[27,28,47,48], large-angle changes have been reported to occur cooperatively as reorganization of the hydrogen bond network.

In water at room temperatures, the thermal fluctuations are large. Thus, we performed 50 independent runs of 60 ps length to produce Figs.9, 10, and 13 and the bottom panels of Fig.12. In this section, $\langle\cdots\rangle$ denotes taking the nonequilibrium average over these 50 runs, which should not be confused with the time average in the previous section.

B. Results of 1D Profiles. In Fig.9, we show 1D profiles of $P(z,t)$ in eq 30 and $\Psi(z,t)$ in eq 31 at $t =$ 0.001, 1.5, and 6 ps. Here, the system is divided into two Stern layers and a bulk region even in transient states. In the bulk region, $P_b(x,t)$ increases continuously, while $E_b(t)$ increases from a negative value ($t < 0$) to a positive value discontinuously at $t = 0$ and then decreases to the final positive value.

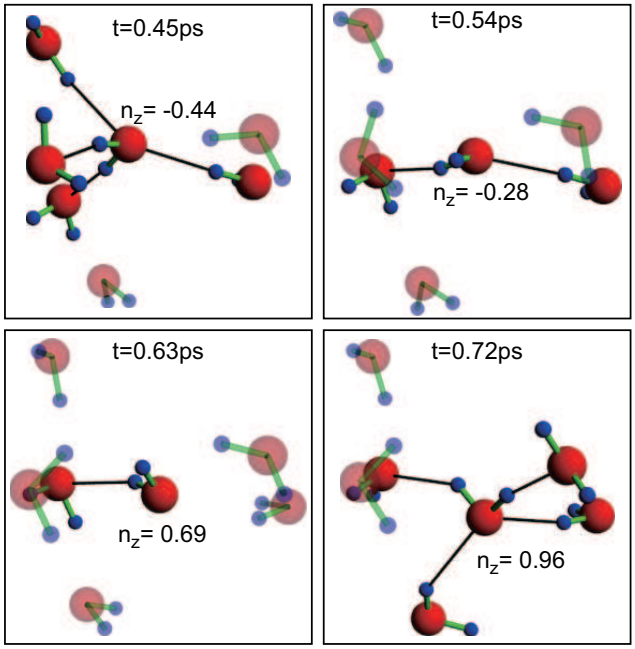

FIG. 8: An example of reorientation dynamics of water molecules at $t = 0.45$, 0.54, 0.63, and 0.72 ps in one run of field reversal, where the z axis is in the vertical direction. Intermolecular hydrogen bonds are also written (black bars). To a molecule at the center, value of $n_z = \cos\theta$ is attached in each panel. The other molecules have been connected by hydrogen-bonding at some t in time interval [0.45 ps,0.72 ps].

In Fig.10, , we give $\langle\bar{\sigma}_0\rangle(t)$, $P_b(t)$, and $\langle M_z\rangle(t)/V$ vs t in (a). Here, eqs 16 and 34 hold, so $4\pi\langle\bar{\sigma}_0\rangle(t)$ increases by 2×0.42 V/nm discontinuously at $t = 0$. These quantities are very close since E_a and $E_b(t)$ are much smaller. In (b), we give the average of the z component of the polarization direction $\bar{n}_k(t)$ in eq 1, denoted by $\langle n_z\rangle(t)$, for the molecules in the three regions $z_{k\mathrm{G}} < 0.1H$, $z_{k\mathrm{G}} > 0.9H$, and $0.1H < z_{k\mathrm{G}} < 0.9H$ separately. The relaxations near the walls and in the bulk are similar because the adsorption is weak in our simulation. Also displayed are $E_b(t)$ in (c) and $\Phi_0^{\mathrm{w}}(t)$ and $\Phi_H^{\mathrm{w}}(t)$ in (d), which become small with considerable fluctuations for $t > 5$ ps. The quantities in (a)-(d) relax exponentially with a common relaxation rate τ_r^{-1} with $\tau_r = 2.84$ ps at long times. In particular, in the inset in (a), this exponential decay can be seen from the beginning in the average polarization difference $\Delta\langle M_z\rangle(t) = \langle M_z\rangle(\infty) - \langle M_z\rangle(t)$.

C. Big Rotational Jumps and Hydrogen-Bonded Clusters. In water, large orientational changes of the dipoles are accompanied by breakage and reorganization of the hydrogen-bond network even at room temperatures[47,48]. This suggests that large angle changes are relevant in the relaxation after a reversal of strong applied field. Thus, we consider largely rotated (LR) molecules with angle jumps determined by

$$n_{zk}(t) - n_{zk}(0) > 0.8, \tag{62}$$

where $n_{zk}(t) = \cos[\theta_k(t)]$ is the z component of the polarization direction $\boldsymbol{n}_k(t)$ in eq 1 with $\theta_k(t)$ being the angle of the polarization with respect to the z axis.

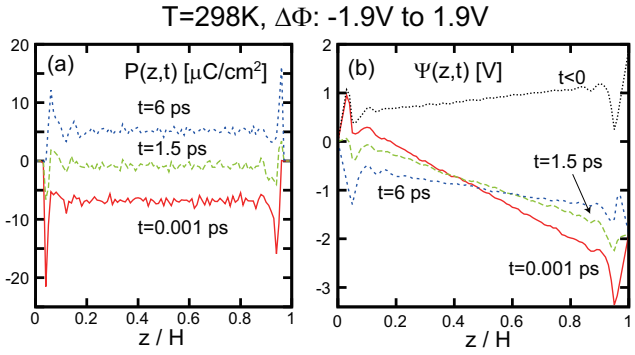

FIG. 9: Space-time-evolution after field reversal from $\Delta\Phi = -1.9$ V to 1.9 V at $T = 298$ K. (a) $P(z,t)$ and (b) $\Psi(z,t)$ at $t = 0.001$, 1.5, and 6 ps. These are averages over 50 runs.

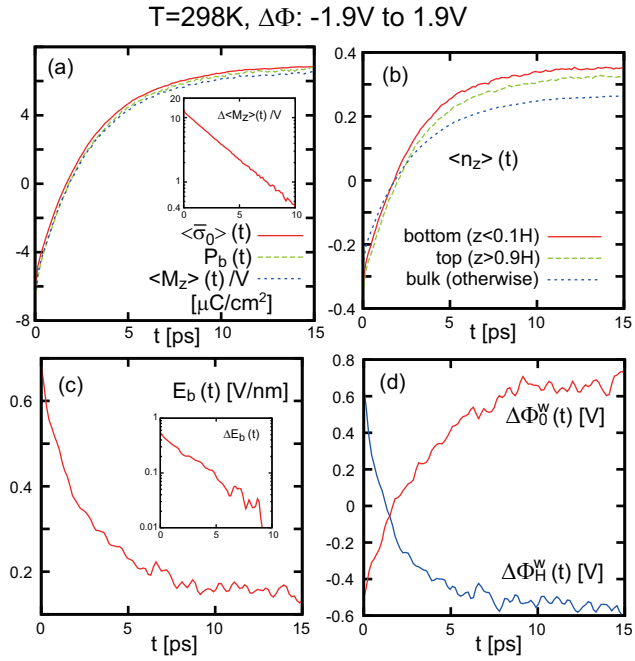

FIG. 10: Time-evolution after field reversal from $\Delta\Phi = -1.9$ V to 1.9 V at $T = 298$ K. (a) $\langle\bar{\sigma}_0\rangle(t)$, $P_b(t)$, and $\langle M_z\rangle(t)/V$ vs t. Inset: $\Delta\langle M_z\rangle(t) = \langle M_z\rangle(\infty) - \langle M_z\rangle(t)$ divided by V on a semi-logarithmic scale. (b) $\langle n_z\rangle(t)$ (average of $n_{zk}(t)$) vs t for molecules in three regions: $z_{k\mathrm{G}} < 0.1H = 4.5$ Å, $z_{k\mathrm{G}} > 0.9H$, and $0.1H < z_{k\mathrm{G}} < 0.9H$. (c) $E_b(t)$ vs t. Inset: $\Delta E_b(t) = E_b(t) - E_b(\infty)$ on a semi-logarithmic scale. (d) $\Delta\Phi_0^{\mathrm{w}}(t)$ and $\Delta\Phi_H^{\mathrm{w}}(t)$ in eq 40 vs t. These are averages over 50 runs.

In Fig.11, we present snapshots of the LR molecules satisfying eq 62 in the left panels at $t = 1.5$ and 3 ps. Among these molecules, we pick up those belonging to hydrogen-bonded clusters with member numbers exceeding 2 in the right panels. In the bottom panels, cross-sectional snapshots at these times are displayed. In these snapshots, large-angle rotational jumps occur

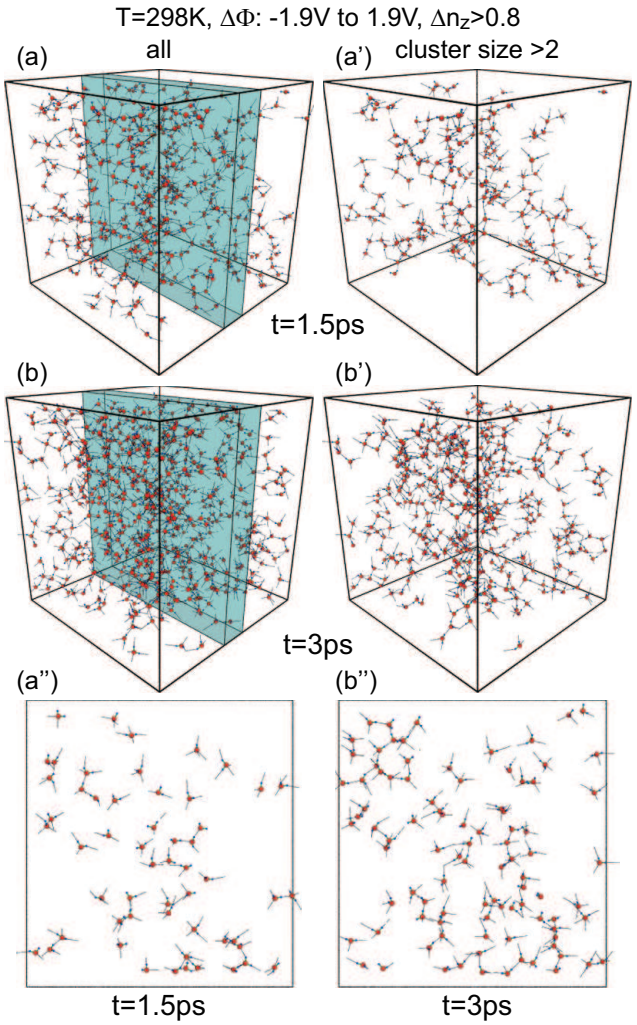

FIG. 11: Largely rotated (LR) molecules with big rotational jumps satisfying eq 62 at (a) $t = 1.5$ and (b) 3 ps (left), among which selected are those forming hydrogen-bonded clusters with sizes exceeding 2 at (a') $t = 1.5$ and (b') 3 ps (right). The z axis is in the vertical direction. Cross-sectional snapshots at (a") $t = 1.5$ and (b") 3 ps (bottom), where displayed are molecules with their centers of mass in the shaded region with thickness 6 Å in (a) and (b).

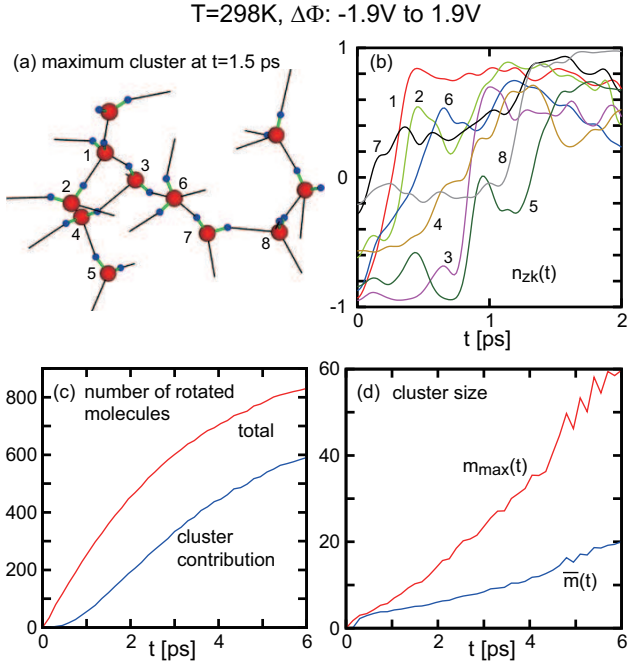

FIG. 12: (a) Snapshot of a hydrogen-bonded cluster whose members undergo big rotational jumps. (b) Time-smoothed trajectories $\bar{n}_{zk}(t)$ in eq 63 for 8 molecules in (a). (c) Number of largely rotated molecules (total) and that of largely rotated molecules belonging to H-bonded clusters with sizes exceeding 2 (cluster contribution) vs t. (d) Average maximum cluster size $m_{\max}(t)$ and mean cluster size $\bar{m}(t)$ vs t. Curves in (c) and (d) are obtained as averages over 50 runs.

collectively and heterogeneously. We show that the LR molecules themselves form hydrogen-bonded clusters, which we have detected by comparing two sets of the orientation configurations at two times. Such dynamic heterogeneities have been detected in translation and rotation in supercooled water[29,30] and in double glass[49].

In Fig.12, we illustrate a cluster composed of 11 LR molecules in (a), which is the largest one at $t = 1.5$ ps in one simulation run. Here, the orientations $\boldsymbol{n}_k(t)$ of these molecules exhibit rapidly varying thermal fluctuations, so we consider the time average of their z components,

$$\bar{n}_{zk}(t) = \int_{t-\Delta t}^{t} dt' n_{zk}(t')/\Delta t. \qquad (63)$$

In (b), setting $\Delta t = 0.015$ ps, we plot $\bar{n}_{zk}(t)$ vs t for 8 members depicted in (a). We can see these molecules undergo simultaneous big rotational jumps in a time interval of 1 ps. In (c), as functions of t, we show the total number of the LR molecules and that of the LR molecules forming hydrogen-bonded clusters with sizes exceeding 2. In (d), we plot the average maximum cluster size $m_{\max}(t)$ and the mean cluster size,

$$\bar{m}(t) = \langle \sum_{m>2} N_m(t) m^2 / \sum_{m>2} N_m(t) m \rangle, \qquad (64)$$

where $N_m(t)$ is the number of the clusters with size m,

D. Big Jump Fraction and Hydrogen-Bond Numbers. We need to quantitatively show how big-jump reorientations can be a dominant mechanism of the relaxation. To this end, we define the big-jump fraction by

$$\phi_M^{\rm jump}(t) = \left\langle \sum_{k\in \rm jump} [n_{zk}(t) - n_{zk}(0)] \right\rangle \frac{\mu_0}{\Delta M(t)}, \qquad (65)$$

where we sum over molecules k satisfying eq 62. In the denominator, we set $\Delta M(t) = \mu_0 \langle \sum_k [n_{zk}(t) - n_{zk}(0)] \rangle$ summing over all k, so it is equal to $\langle M_z \rangle(t) - \langle M_z \rangle(0)$ (see Fig.11(a) for its time dependence). In Fig.13(a), $\phi_M^{\rm jump}(t)$ is small at very short times but soon exceeds

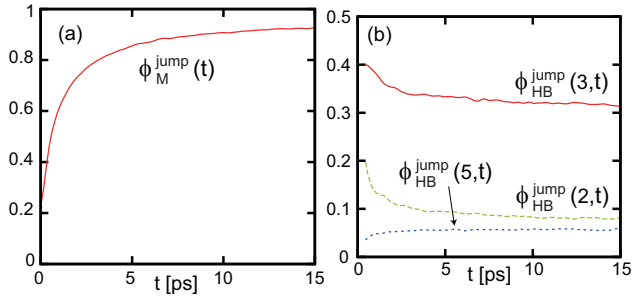

FIG. 13: (a) Big-jump fraction $\phi_M^{\rm jump}(t)$ in eq 65 vs t, which is the fraction of the contribution of LR molecules to $\langle M_z\rangle(t) - \langle M_z\rangle(0)$. (b) Fractions $\phi_{\rm HB}^{\rm jump}(m,t)$ vs t with hydrogen bond number $m = 2, 3$ and 5. These are averages over 50 runs.

0.6 for $t > 1$ ps. Therefore, the relaxation is governed by big rotational jumps for $t > 1$ ps.

The reorganization of the hydrogen bond network occurs very rapidly, so it is a difficult task to capture the dynamics quantitatively[39,48]. Here, we consider the hydrogen bond number m_k for molecule k, which is ideally 4 (two for its oxygen atom and two for its protons) for the tetrahedral structure. Due to structural disorder, however, its thermal average becomes $\langle m_k\rangle \cong 3.6$ at $T = 298$ K for our definition of hydrogen bonds. In Fig.13(b), we plot the fractions $\phi_{\rm HB}^{\rm jump}(m,t)$ of the LR molecules with $m_k = m$ at time t. They are expressed as

$$\phi_{\rm HB}^{\rm jump}(m,t) = \Big\langle \sum_{k\in {\rm jump}} \delta_{m m_k(t)}/N_{\rm jump}(t) \Big\rangle, \qquad (66)$$

where $N_{\rm jump}(t)$ is the number of the LR molecules satisfying eq 62 at time t. We can see that $\phi_{\rm HB}^{\rm jump}(3,t)$ and $\phi_{\rm HB}^{\rm jump}(2,t)$ decay from 0.40 and 0.20 at $t = 0.4$ ps to the equilibrium values $\phi_{\rm HB}(3) = 0.31$ and $\phi_{\rm HB}(2) = 0.09$, respectively, with a relaxation time about 2 ps. There is almost no change in $\phi_{\rm HB}^{\rm jump}(5,t)$ from the equilibrium value $\phi_{\rm HB}(5) = 0.060$. Note that $\phi_{\rm HB}(4) \cong 0.54$ in equilibrium. Thus, the nonequilibrium distribution $\phi_{\rm HB}^{\rm jump}(m,t)$ rapidly approaches the equilibrium distribution $\phi_{\rm HB}(m)$ on a timescale of 2 ps and the deviation $\phi_{\rm HB}^{\rm jump}(m,t) - \phi_{\rm HB}(m)$ is not large except for very small $t(< 0.1$ ps), though a few hydrogen bonds are broken for each big rotational jump.

V. SUMMARY AND REMARKS

In this paper, we have studied dielectric responses in applied electric field and polarization relaxation after field reversal in a system of 2400 water molecules between metal walls at $z = 0$ and $H = 44.7$Å. We have used the TIP4P/2005 model and the 3D Ewald method, including the image effect to realize the constant potential condition on the walls. In the following, we summarize our main results with critical remarks.

(i) In Sec.II, we have explained our simulation method. We have shown that the surface charges yield an electric potential consisting of the average part $-4\pi\bar\sigma_0 z$ and a deviation ϕ_s, where $\bar\sigma_0$ is the mean surface charge at $z = 0$. Then, each charge i is acted by the field from the surface charges and the dipolar field $\boldsymbol{E}_i^d$ from the other charges in the cell. We have expressed the electrostatic potential $U_{\rm m}$ in terms of ϕ_s in eq 23 not using the image charges. If ϕ_s is negligible, we can justify the simulation methods by Yeh and Berkowitz[13] and by Petersen *et al.*[18]. Since E_a appears linearly in $U_{\rm m}$, we can derive the linear response expressions such as that for $\varepsilon_{\rm eff}$ in eq 36.

(ii) In Sec.IIIA, we have calculated the 2D structure factors $S_0(k)$ and $S_H(k)$ and the corresponding 2D pair correlation functions $g_0(\rho)$ and $g_H(\rho)$ for the surface charge fluctuations at the top and the bottom in Fig.2. We have shown that $\phi_s(\boldsymbol{r}) \to 0$ far from the walls in Fig.3. In Appendix C, we have examined how the fluctuation amplitude $e_s(z) = [\langle|\nabla\phi_s|^2\rangle]^{1/2}$ decays far from the walls. Therefore, the bulk properties of water in applied electric field are determined by the mean surface charge $\bar\sigma_0$[13,18]. On the other hand, the molecules near a metal wall are under influence of strongly heterogeneous surface charges. Thus, the molecules near and far from the walls behave very differently.

(iii) In Sec.IIIB, we have examined average 1D profiles using the microscopic expression for the polarization density $\boldsymbol{p}(\boldsymbol{r})$ in Appendix A, where Stern layers with thickness $d = 4.7$ Å and a homogeneous bulk region appear. The ratio between the polarization P_b and the electric field E_b in the bulk yields the dielectric constant $\varepsilon = 1 + 4\pi P_b/E_b$. The applied field E_a is larger than E_b by $E_a/E_b = 1 + \ell_{\rm w}/H$, where $\ell_{\rm w}$ is a surface electric length about 10 nm. Thus, the dielectric response strongly depends on the cell length H. In the previous simulations[8,9,13,14], H has been shorter than $\ell_{\rm w}$.

(iv) Furthermore, in Sec.IIIB, we have examined the zero-field surface potential drop $\Phi_{00}^{\rm w}$ dividing the Stern layer into two layers. We have found that the polarization is downward (upward) in the first (second) layer for $\Delta\Phi = 0$. The H-down orientation in Fig.1 is preferred in the first layer due to the image interaction, while a surface-to-bulk crossover takes place in the hydrogen bonding in the second layer. In our case, the water adsorption is weak and the polarization in the first layer is relatively small compared to that in the second, leading to $\Phi_{00}^{\rm w} \sim -0.09$ V. For strong adsorption, a positive $\Phi_{00}^{\rm w}$ follows[14].

(v) In Sec.IIIC, we have visualized clustering of the hydrogen bonds in the Stern layer. The hydrogen bond orientations in the Stern layer tend to be parallel to the walls as in Fig.5(c). Large-scale density fluctuations near the walls have also been detected in Fig.5(d). These mesoscopic heterogeneities result from competition between hydrogen bond formation and packing near a wall[34,35,43].

(vi) In Sec.IIID, we have calculated the local field $\boldsymbol{E}_k^{\rm loc}$ on each molecule k using its microscopic expression in Appendix B. Writing the bulk average of its z component

as $E_{\rm loc} = E_b + 4\pi\gamma_{\rm loc}P_b$, we have obtained the Lorentz factor $\gamma_{\rm loc} \cong 0.58$. Its deviation from the classical value 1/3 is caused by the surrounding nearby molecules. The local field exhibits large fluctuations with amplitude of order $e/\sigma^2 \sim 15$ V/nm with $\sigma = 3.2$ Å and its distribution is deformed by applied field as in Fig.6(a). We note that the dipolar energy $\mu_0 e/\sigma^2 = 26 k_B T$ per molecule is very large and the dipole moment $\boldsymbol{\mu}_k$ should be mostly along the local field $\boldsymbol{E}_k^{\rm loc}$. This aspect will be investigated in future.

(vii) In Sec.IIIE, we have confirmed that the local field contribution from the exterior of a nanometer sphere $\boldsymbol{E}_k^{\rm out}$ is given by its continuum limit $(E_b + 4\pi P_b/3)\boldsymbol{e}_z$ with small deviations obeying a Gaussian distribution. On the other hand, the contribution from the sphere interior $\boldsymbol{E}_k^{\rm in} = \boldsymbol{E}_k^{\rm loc} - \boldsymbol{E}_k^{\rm out}$ exhibits large fluctuations ($\sim e/\sigma^2$), where relevant is the short-range orientational correlation. In Sec.IIIF, we have furthermore divided the dipolar field from the molecules in the cell into long-range and short-range parts as $\boldsymbol{E}_k^{\rm d} = \boldsymbol{E}_k^{{\rm d}\ell} + \boldsymbol{E}_k^{\rm ds}$ using the Coulomb potential division $1/r = \psi_\ell(r) + \psi_s(r)$ in the Ewald method. We have found that a main contribution to the long-range part $\boldsymbol{E}_k^{{\rm d}\ell}$ is produced by the dipoles near the walls and can well be approximated by its continuum limit. With the aid of these two field divisions, we can investigate how the continuum description can be used in the calculation of the long-range interaction.

(viii) In Sec.IV, we have studied the orientation dynamics after field reversal. Due to the presence of the hydrogen bond network, the relaxation is governed by large-angle rotational jumps[47,48], as demonstrated in Figs.11-13. These big jumps occur in the form of hydrogen-bonded clusters and the resultant dynamic heterogeneity has been displayed in Fig.11. We have examined how these big jumps contribute to the polarization relaxation in Fig.13(a). The threefold and fivefold hydrogen bonds transiently increase right after big jumps as in Fig.13(b). Note that cooperative motions are more conspicuous with smaller thermal noises in supercooled water[29,30]. Generally in supercooled anisotropic liquids, dynamic heterogeneity emerges both in rotational and translational motions[49].

Acknowledgments

This work was supported by KAKENHI (Nos. 25610122 and 25000002). The numerical calculations were carried out on SR16000 at YITP in Kyoto University.

Appendix A: Local Electric Field in Water

In the TIP4P/2005 model[31], a water molecule is treated as a rigid isosceles triangle. For a molecule k, we write the positions of its oxygen atom and two protons as $\boldsymbol{r}_{k\rm O}$, $\boldsymbol{r}_{k\rm H1}$, and $\boldsymbol{r}_{k\rm H2}$, respectively. Here, $a_{\rm OH} = |\boldsymbol{r}_{k\rm H1} - \boldsymbol{r}_{k\rm O}| = |\boldsymbol{r}_{k\rm H2} - \boldsymbol{r}_{k\rm O}| = 0.957$ Å and the angle between $\boldsymbol{r}_{k\rm H1} - \boldsymbol{r}_{k\rm O}$ and $\boldsymbol{r}_{k\rm H2} - \boldsymbol{r}_{k\rm O}$ is $\theta_{\rm HOH} = 104.5°$, so $a_{\rm HH} = |\boldsymbol{r}_{k\rm H1} - \boldsymbol{r}_{k\rm H2}| = 2a_{\rm OH}\sin(\theta_{\rm HOH}/2) = 0.844$ Å. For each molecule, the charges are at the proton positions with $q_{\rm H} = 0.5564e$ and at another position M,

$$\boldsymbol{r}_{k\rm M} = \boldsymbol{r}_{k\rm O} + a_{\rm OM}\boldsymbol{n}_k \tag{A1}$$

with $q_{\rm M} = -2q_{\rm H}$ and $a_{\rm OM} = 0.1546$Å. The elementary charge is $e = 23.82(\epsilon\sigma)^{1/2}$. The $\boldsymbol{n}_k$ is the unit vector from $\boldsymbol{r}_{k\rm O}$ to the midpoint of the proton positions,

$$\bar{\boldsymbol{r}}_{k\rm H} = \frac{1}{2}(\boldsymbol{r}_{k\rm H1} + \boldsymbol{r}_{k\rm H2}). \tag{A2}$$

Thus, $\bar{\boldsymbol{r}}_{k\rm H} - \boldsymbol{r}_{k\rm O} = a_{\rm d}\boldsymbol{n}_k$ with $a_{\rm d} = a_{\rm OH}\cos(\theta_{\rm HOH}/2) = 0.5859$Å. The dipole is expressed as in eq 1 with $\mu_0 = 2q_{\rm H}(a_{\rm d} - a_{\rm OM}) = 3.62(\epsilon\sigma^3)^{1/2} = 2.305$ D.

Next, we shift the charge positions $\boldsymbol{r}_j$ infinitesimally by $d\boldsymbol{r}_j$ with the molecular shape held unchanged. Their images outside the cell are also shifted by the same amounts. The change in the electrostatic energy in eq 8 is rewritten at fixed E_a as

$$dU_{\rm m} = -\sum_k [\boldsymbol{F}_k^e \cdot d\boldsymbol{r}_{k\rm G} + \boldsymbol{F}_k^r \cdot d\boldsymbol{\xi}_k + \boldsymbol{E}_k^{\rm loc} \cdot d\boldsymbol{\mu}_k]. \tag{A3}$$

where we introduce the center of mass and the relative positional vector between two protons by

$$\boldsymbol{r}_{k\rm G} = \frac{8}{9}\boldsymbol{r}_{k\rm O} + \frac{1}{18}(\boldsymbol{r}_{k\rm H1} + \boldsymbol{r}_{k\rm H2}), \tag{A4}$$

$$\boldsymbol{\xi}_k = \boldsymbol{r}_{k\rm H1} - \boldsymbol{r}_{k\rm H2}. \tag{A5}$$

For each water molecule k, the conjugate electric forces to $\boldsymbol{r}_{k\rm G}$ and $\boldsymbol{\xi}_k$ are given by

$$\boldsymbol{F}_k^e = q_{\rm H}(\boldsymbol{E}_{k\rm H1} + \boldsymbol{E}_{k\rm H2} - 2\boldsymbol{E}_{k\rm M}), \tag{A6}$$

$$\boldsymbol{F}_k^r = \frac{1}{2}q_{\rm H}(\boldsymbol{E}_{k\rm H1} - \boldsymbol{E}_{k\rm H2}). \tag{A7}$$

The $\boldsymbol{E}_k^{\rm loc}$ in eq A3 is the local electric field on water molecule k, which is conjugate to $\boldsymbol{\mu}_k$. It is expressed as in eq 48 with $b_{\rm M} = (a_{\rm OM} - a_{\rm d}/9)/(a_{\rm d} - a_{\rm OM}) = 0.208$.

Appendix B: Microscopic Expressions for Polarization Density and Poisson Electric Potential

We give a microscopic expression for the polarization density $\boldsymbol{p}(\boldsymbol{r})$ in terms of the charged positions $\boldsymbol{r}_j$ for polar molecules (with $\sum_j q_j = 0$). We assume that $\boldsymbol{p}$ is related to the microscopic charge density $\rho(\boldsymbol{r})$ by

$$-\nabla \cdot \boldsymbol{p} = \rho = \sum_j q_j \delta(\boldsymbol{r} - \boldsymbol{r}_j). \tag{B1}$$

We introduce the following 3D symmetrized δ-function,

$$\hat{\delta}(\boldsymbol{r}; \boldsymbol{r}_1, \boldsymbol{r}_2) = \int_0^1 d\lambda\ \delta(\boldsymbol{r} - \lambda\boldsymbol{r}_1 - (1-\lambda)\boldsymbol{r}_2), \tag{B2}$$

where $\boldsymbol{r}_1$ and $\boldsymbol{r}_2$ are particle positions. This δ-function is nonvanishing only on the line segment connecting $\boldsymbol{r}_1$

and $\boldsymbol{r}_2$. It is known to appear in the microscopic expression for the local stress tensor[50]. For the TIP4P/2005 model[31], using the relation $(\boldsymbol{r}_1-\boldsymbol{r}_2)\cdot\nabla\hat{\delta}(\boldsymbol{r};\boldsymbol{r}_1,\boldsymbol{r}_2) = \delta(\boldsymbol{r}-\boldsymbol{r}_2)-\delta(\boldsymbol{r}-\boldsymbol{r}_1)$, we find $\boldsymbol{p}$ explicitly as

$$\boldsymbol{p}(\boldsymbol{r}) = \sum_k \frac{q_H}{2}\left[\hat{\delta}(\boldsymbol{r};\boldsymbol{r}_{kH1},\bar{\boldsymbol{r}}_{kH}) - \hat{\delta}(\boldsymbol{r};\boldsymbol{r}_{kH2},\bar{\boldsymbol{r}}_{kH})\right]\boldsymbol{\xi}_k + \sum_k \hat{\delta}(\boldsymbol{r};\bar{\boldsymbol{r}}_{kH},\boldsymbol{r}_{kM})\boldsymbol{\mu}_k, \tag{B3}$$

where $\bar{\boldsymbol{r}}_{kH}$, $\boldsymbol{\xi}_k$, and $\boldsymbol{\mu}_k$ are defined by eqs A2, A5, and 1, respectively. We then find the total polarization $\boldsymbol{M} = \int d\boldsymbol{r}\boldsymbol{p}(\boldsymbol{r}) = \sum_k \boldsymbol{\mu}_k$. Without ions, the electric field $\boldsymbol{E} = -\nabla\Phi$ away from the charge positions satisfies

$$\nabla\cdot(\boldsymbol{E}+4\pi\boldsymbol{p}) = 0. \tag{B4}$$

We obtain eq 16 by multiplying z to the above relation and integrating in the cell.

To calculate the average polarization $P(z)$ in eq 30, we introduce the laterally integrated polarization,

$$M_\perp(z) = \int dxdy\ p_z(\boldsymbol{r}). \tag{B5}$$

Then, $P(z) = \langle p_z(\boldsymbol{r})\rangle = \langle M_\perp(z)\rangle/L^2$. The total polarization along the z axis in eq 9 is given by $M_z = \int_0^H dz M_\perp(z)$. This $M_\perp(z)$ is obtained from eq B3 if we replace $\hat{\delta}(\boldsymbol{r};\boldsymbol{r}_1,\boldsymbol{r}_2)$ by the 1D symmetrized δ-function,

$$\int_0^1 d\lambda\ \delta(z-\lambda z_1-(1-\lambda)z_2) = [\theta(z-z_1)-\theta(z-z_2)]/(z_2-z_1), \tag{B6}$$

where $\theta(u)$ is the step function. We then find

$$M_\perp(z) = -q_H\sum_k[\theta(z-z_{kH1})+\theta(z-z_{kH2}) -2\theta(z-z_{kM})], \tag{B7}$$

which leads to eq 30.

Appendix C: Behavior of $e_s(z)$ away from Walls

Using eq 29 we discuss the behavior of the fluctuation amplitude $e_s(z)$ of the electric field due to the surface charge deviations away from the walls. For $z \gg \xi_{s0}$ and $H-z \gg \xi_{sH}$, we can replace $S_{\lambda k}$ by $S_{\lambda 0} = \lim_{k\to 0} S_{\lambda k}$.

First, if $L/4\pi < H$, we consider the region with $z \gtrsim L/4\pi$ and $H-z \gtrsim L/4\pi$, where we pick up the contributions from the smallest $k = 2\pi/L$ to obtain

$$e_s(z)^2 \cong \frac{32\pi^2}{L^2}\sum_{\lambda=0,H} S_{\lambda 0}\exp[-4\pi|z-\lambda|/L]. \tag{C1}$$

In fact, in Fig.3(c), the right hand side is 70% of the numerical value at $z = H/2$.

Second, we consider the thin film limit $L/4\pi \gg H \gg \xi_{s\lambda}$, though this is not the case for our cell with $L = H$. In this case, we may replace $2\pi L^{-2}\sum_{\boldsymbol{k}\neq\boldsymbol{0}}$ by the integral $\int_0^\infty dkk$ (with k being continuous) to obtain

$$e_s(z)^2 \cong \pi S_{00}/z^2 + \pi S_{H0}/(H-z)^2. \tag{C2}$$

From this relation, we estimate $e_s(H/2) \sim 0.1e/H\sigma \sim 1.5(\sigma/H)$ [V/nm] on the film midplane $z = H/2$, where σ is the molecular size(~ 3 Å).

[1] Allen, M. P.; Tildesley, D. J. *Computer Simulation of Liquids*; Clarendon Press: Oxford, 1987.

[2] de Leeuw, S. W.; Perram, J. W.; Smith, E. R. Simulation of Electrostatic Systems in Periodic Boundary Conditions. I. Lattice Sums and Dielectric Constants. Proc. R. Soc. Lond. A **1980**, *373*, 27-56.

[3] Weis, J.-J; Levesque, D. Simple Dipolar Fluids as Generic Models for Soft Matter. Adv. Polym. Sci. **2005**, *185*, 163-225.

[4] Parry, D. E. The Electrostatic Potential in the Surface Region of an Ionic Crystal. Surf. Sci. **1975**, *49*, 433-440.

[5] Heyes, D. M.; Barber, M.; Clarke, J. H. R. Molecular Dynamics Computer Simulation of Surface Properties of Crystalline Potassium Chloride. J. Chem. Soc., Faraday Trans. 2 **1977**, *73*, 1485-1496.

[6] de Leeuw, S. W.; Perram, J. W. Statistical Mechanics of Two-dimensional Coulomb Systems: II. The Two-dimensional One-component Plasma. Physica A **1982**, *113*, 546-558.

[7] Smith, E. R. Electrostatic Potentials for Simulations of Thin Layers. Mol. Phys. **1988**, *65*, 1089-1104.

[8] Yeh, I.-C.; Berkowitz, M. L. Dielectric Constant of Water at High Electric Fields: Molecular Dynamics Study. J. Chem. Phys. **1999**, *110*, 7935-7942.

[9] Hautman, J.; Halley, J. W.; Rhee, Y.-J. Molecular Dynamics Simulation of Water between Two Ideal Classical Metal Walls. J. Chem. Phys. **1989**, *91*, 467-472.

[10] Perram, J. W.; Ratner, M. A. Simulations at Conducting Interfaces: Boundary Conditions for Electrodes and Electrolytes. J. Chem. Phys. **1996**, *104*, 5174-5180.

[11] Klapp, S. H. L. Monte-Carlo Simulations of Strongly Interacting Dipolar Fluids between Two Conducting Walls. Mol. Simul. **2006**, *32*, 609-621.

[12] Takae, K.; Onuki, A. Applying Electric Field to Charged and Polar Particles between Metallic Plates: Extension of the Ewald Method. J. Chem. Phys. **2013**, *139*, 124108.

[13] Yeh, I.-C.; Berkowitz, M. L. Ewald Summation for Systems with Slab Geometry. J. Chem. Phys. **1999**, *111*, 3155-3162.

[14] Willard, A. P.; Reed, S. K.; Madden, P. A.; Chandler, D. Water at an Electrochemical Interface - a Simulation Study. Faraday Discuss. **2009**, *141*, 423-441.

[15] Shelley, J. C.; Patey, G. N. Boundary Condition Effects in Simulations of Water Confined between Planar Walls. Mol. Phys. **1996**, *88*, 385-398.

[16] Siepmann, J. I.; Sprik, M. Influence of Surface Topology and Electrostatic Potential on Water/Electrode Systems.

J. Chem. Phys. **1995**, *102*, 511-524.
[17] Reed, S. K.; Lanning, O. J.; Madden, P. A. Electrochemical Interface between an Ionic Liquid and a Model Metallic Electrode. J. Chem. Phys. **2007**, *126*, 084704.
[18] Petersen, M. K.; Kumar, R.; White, H. S. ; Voth, G. A. A Computationally Efficient Treatment of Polarizable Electrochemical Cells Held at a Constant Potential. J. Phys. Chem. C **2012**, *116*, 4903-4912.
[19] Thiel, P. A.; Madey, T. E. The Interaction of Water with Solid Surfaces: Fundamental Aspects. Surf. Sci. Rep. **1987**, *7*, 211-385.
[20] Henderson, M. A. The Interaction of Water with Solid Surfaces: Fundamental Aspects Revisited. Surf. Sci. Rep. **2002**, *46*, 1-308.
[21] Schnur, S.; Groβ, A. Properties of Metal-Water Interfaces Studied from First Principles. New J. Phys. **2009**, *11*, 125003.
[22] Parsons, R. The Metal-Liquid Electrolyte Interface. Solid State Ionics **1997**, *94*, 91-98.
[23] Behrens, S. H.; Grier, D. G. The Charge of Glass and Silica Surfaces. J. Chem. Phys. **2001**, *115*, 6716-6721.
[24] Fröhlich, H. *Theory of dielectrics*; Oxford University Press: Oxford, 1949.
[25] Onsager, L. Electric Moments of Molecules in Liquids. J. Am. Chem. Soc. **1936**, *58*, 1486-1493.
[26] Kirkwood, J. G. The Dielectric Polarization of Polar Liquids. J. Chem. Phys. **1939**, *7*, 911-919.
[27] Tanaka, H.; Ohmine, I. Large Local Energy Fluctuations in Water. J. Chem. Phys. **1987**, *87*, 6128-6139.
[28] Tanaka, H.; Ohmine, I. Potential Energy Surfaces for Water Dynamics: Reaction Coordinates, Transition States, and Normal Mode Analyses. J. Chem. Phys. **1989**, *91*, 6318-6327.
[29] Giovambattista, N.; Buldyrev, S. V.; Starr, F. W.; Stanley, H. E. Connection between Adam-Gibbs Theory and Spatially Heterogeneous Dynamics. Phys. Rev. Lett. **2003**, *90*, 085506.
[30] Mazza, M. G.; Giovambattista, N.; Starr, F. W.; Stanley, H. E. Relation between Rotational and Translational Dynamic Heterogeneities in Water. Phys. Rev. Lett. **2006**, *96*, 057803.
[31] Abascal, J. L. F.; Vega, C. A General Purpose Model for the Condensed Phases of Water: TIP4P/2005. J. Chem. Phys. **2005**, *123*, 234505.
[32] Yu, H.; van Gunsteren, W. F. Accounting for Polarization in Molecular Simulation. Compt. Phys. Commun. **2005**, *172*, 69-85.
[33] Gonzalez, M.A.; Abascal, J. L. F. A Flexible Model for Water Based on TIP4P/2005. J. Chem. Phys. **2011**, *135*, 224516.
[34] Lee, C. Y.; McCammon, J. A.; Rossky, P. J. The Structure of Liquid Water at an Extended Hydrophobic Surface. J. Chem. Phys. **1984**, *80*, 4448-4455.
[35] Raghavan, K; Foster, K; Motakabbir, K; Berkowitz, M. Structure and Dynamics of Water at the Pt(111) Interface: Molecular Dynamics Study. J. Chem. Phys. **1991**, *94*, 2110-2117.
[36] Kathmann, S. M.; Kuo, I.-F. W.; Mundy, C. J.; Schenter, G. K. Understanding the Surface Potential of Water. J. Phys. Chem. B **2011**, *115*, 4369-4377.
[37] Neumann, M. Dipole Moment Fluctuation Formulas in Computer Simulations of Polar Systems. Mol. Phys. **1983**, *50*, 841-858.
[38] Höchtl, P.; Boresch, S.; Bitomsky, W.; Steinhauser, O. Rationalization of the Dielectric Properties of Common Three-Site Water Models in Terms of their Force Field Parameters. J. Chem. Phys. **1998**, *109*, 4927-4937.
[39] Luzar, A.; Chandler, D. Effect of Environment on Hydrogen Bond Dynamics in Liquid Water. Phys. Rev. Lett. **1996**, *76*, 928-931.
[40] Zielkiewicz, J. Structural Properties of Water: Comparison of the SPC, SPCE, TIP4P, and TIP5P Models of Water. J. Chem. Phys. **2005**, *123*, 104501.
[41] Kumar, R.; Schmidt, J. R.; Skinner, J. L. Hydrogen Bonding Definitions and Dynamics in Liquid Water. J. Chem. Phys. **2007**, *126*, 204107.
[42] Prada-Gracia, D.; Shevchuk, R.; Rao, F. The Quest for Self-Consistency in Hydrogen Bond Definitions. J. Chem. Phys. **2013**, *139*, 084501.
[43] Bratko, D.; Daub, C. D.; Leung, K.; Luzar, A. Effect of Field Direction on Electrowetting in a Nanopore. J. Am. Chem. Soc. **2007**, *129*, 2504-2510.
[44] Smith, J. D.; Saykally, R. J.; Geissler, P. L. The Effects of Dissolved Halide Anions on Hydrogen Bonding in Liquid Water. J. Am. Chem. Soc. **2007**, *129*, 13847-13856.
[45] Reischl, B.; Köfinger, J.; Dellago, C. The Statistics of Electric Field Fluctuations in Liquid Water. Mol. Phys. **2009**, *107*, 495-502.
[46] Sellner, B.; Valiev, M.; Kathmann, S. M. Charge and Electric Field Fluctuations in Aqueous NaCl Electrolytes. J. Phys. Chem. B **2013**, *117*, 10869-10882.
[47] Laage, D.; Stirnemann, G.; Sterpone, F.; Rey, R.; Hynes, J. T. Reorientation and Allied Dynamics in Water and Aqueous Solutions. Annu. Rev. Phys. Chem. **2011**, *62*, 395-416.
[48] Laage, D.; Hynes, J. T. On the Molecular Mechanism of Water Reorientation. J. Phys. Chem. B **2008**, *112*, 14230-14242.
[49] Takae, K; Onuki, A. Formation of Double Glass in Binary Mixtures of Anisotropic Particles: Dynamic Heterogeneities in Rotations and Displacements. Phys. Rev. E **2013**, *88*, 042317.
[50] Onuki, A. *Phase Transition Dynamics*; Cambridge University Press: Cambridge, 2002.